1. Report No.	2. Government Accession No.	3. Recipient's Catalog No.
NASA TN D-7936		

4. Title and Subtitle	5. Report Date
THEORETICAL AERODYNAMICS OF UPPER-SURFACE-BLOWING JET-WING INTERACTION	November 1975
	6. Performing Organization Code

7. Author(s)	8. Performing Organization Report No.
C. Edward Lan and James F. Campbell	L-10037
	10. Work Unit No. 505-06-11-05

9. Performing Organization Name and Address	11. Contract or Grant No.
NASA Langley Research Center Hampton, Va. 23665	

12. Sponsoring Agency Name and Address	13. Type of Report and Period Covered
National Aeronautics and Space Administration Washington, D.C. 20546	Technical Note
	14. Sponsoring Agency Code

15. Supplementary Notes

C. Edward Lan is Associate Professor in the Aerospace Engineering Department at the University of Kansas, Lawrence, Kansas.

16. Abstract

A linear, inviscid subsonic compressible flow theory is formulated to treat the aerodynamic interaction between the wing and an inviscid upper-surface-blowing (USB) thick jet with Mach number nonuniformity. The predicted results showed reasonably good agreement with some available lift and induced-drag data. It was also shown that the thin-jet-flap theory is inadequate for the USB configurations with thick jet.

Additional theoretical results showed that the lift and induced drag were reduced by increasing jet temperature and increased by increasing jet Mach number. Reducing jet aspect ratio, while holding jet area constant, caused reductions in lift, induced drag, and pitching moment at a given angle of attack but with a minimal change in the curve of lift coefficient against induced-drag coefficient. The jet-deflection effect was shown to be beneficial to cruise performance. The aerodynamic center was shifted forward by adding power or jet-deflection angle. Moving the jet away from the wing surface resulted in rapid changes in lift and induced drag. Reducing the wing span of a rectangular wing by half decreased the jet-circulation lift by only 24 percent at a thrust coefficient of 2.

17. Key Words (Suggested by Author(s))

Upper surface blowing
Theoretical jet-wing interaction

18. Distribution Statement

Unclassified – Unlimited

Subject Category 02

THEORETICAL AERODYNAMICS OF UPPER-SURFACE-BLOWING JET-WING INTERACTION

C. Edward Lan* and James F. Campbell
Langley Research Center

SUMMARY

A linear, inviscid subsonic compressible flow theory is formulated to treat the aerodynamic interaction between the wing and an inviscid upper-surface-blowing (USB) thick jet with Mach number nonuniformity. The predicted results showed reasonably good agreement with some available lift and induced-drag data. It was also shown that the thin-jet-flap theory is inadequate for the USB configurations with thick jet.

Additional theoretical results showed that the lift and induced drag were reduced by increasing jet temperature and increased by increasing jet Mach number. Reducing jet aspect ratio, while holding jet area constant, caused reductions in lift, induced drag, and pitching moment at a given angle of attack but with a minimal change in the curve of lift coefficient against induced-drag coefficient. The jet-deflection effect was shown to be beneficial to cruise performance. The aerodynamic center was shifted forward by adding power or jet-deflection angle. Moving the jet away from the wing surface resulted in rapid changes in lift and induced drag. Reducing the wing span of a rectangular wing by half decreased the jet-circulation lift by only 24 percent at a thrust coefficient of 2.

INTRODUCTION

Recently, the feasibility of using the upper-surface-blowing (USB) concept for short take-off and landing operations has been under extensive experimental investigation (refs. 1 to 7). Some of these experimental results have been summarized in a recent paper by Johnson and Phelps (ref. 8). These experimental investigations confirmed the promising aerodynamic and noise characteristics of the USB configurations at low speeds under high lift conditions. On the other hand, several studies, such as references 9 and 10, have indicated that design for good low-speed performance, for example, spanwise spreading into a thinner jet for good jet turning, would appreciably compromise the cruise performance. Additional information about the jet influence is needed, therefore, to provide the designer more choices in his trade-off study. Although the USB concept has been in existence for quite a while, only a few limited theoretical methods have been developed to describe the associated aerodynamic phenomena.

---

*Associate Professor in the Aerospace Engineering Department at the University of Kansas, Lawrence, Kansas.

Experimental evidence shows that the USB jet flow is much more concentrated than that associated with the external-blown-flap (EBF) configuration. It is well known that the conventional thin jet flap is much more effective in producing the lift for a given total jet momentum if the blowing jet has been spread out over a large spanwise distance. This fact may explain some success in predicting the lift characteristics of the EBF configuration by thin-jet-flap theory (ref. 11). The high lift capability of the USB configuration, however, can hardly be explained with the thin-jet-flap theory, because the jet span of the USB configuration tends to be relatively narrow and the jet is thick. Some calculations using the thin-jet-flap theory with the narrow jet span showed that it consistently underestimated the measured lift for the USB configurations.

Original USB concepts, similar to the one in reference 12, had jet thicknesses at the jet exit that were relatively small, less than 2 percent of the local chord. In recent experiments jet thicknesses were examined which were greater than 10 percent of the local chord, a result of simulating the modern or future high-bypass-ratio turbofan engines. With a jet-flow region of finite thickness and of higher dynamic pressure than the free stream, it is not unusual that additional lift would be induced on the neighboring lifting surfaces. This fact has long been recognized by Küchemann and Weber (ref. 13). Physically, the wing-induced flow field will be modified by the jet region and the jet flow will be perturbed because of the presence of the wing. It is the neglect of this wing-jet interaction process which may account for the underprediction of lift by the thin-jet-flap theory.

Historically, the interaction between two flow fields with different energy levels has been concerned with the wing-propeller slipstream interaction problems. Some success in numerical computation has been reported. (See, for example, refs. 14 and 15.) Except for the study of reference 15, the Mach number effect has usually been neglected. Since in the wing-jet interaction problem, as being considered here, the jet Mach number can be different from the free-stream value (Mach number nonuniformity), the theoretical formulations similar to that of reference 14 cannot be conveniently used. Instead, the formulation of reference 15 will be adopted here.

The purposes of this paper are, therefore: (1) to present a thick-jet-wing interaction theory which accounts for differences between the jet and free-stream Mach numbers, (2) to apply this theory to predicting the aerodynamic characteristics of USB configurations, and (3) to investigate theoretically the effects of some configuration and jet parameters. Linear, inviscid subsonic compressible flow theory will be assumed. The effects of wing thickness, nacelle, and fuselage have not been included in the analysis.

SYMBOLS

Values are given in both SI and U.S. Customary Units. The measurements and calculations were made in U.S. Customary Units.

AR	wing aspect ratio
AR_j	jet aspect ratio
A_j	jet cross-sectional area, m^2 (ft^2)
$\vec{a}$	$= (x_1 - x)\vec{i} + (y_1 - y)\vec{j} + (z_1 - z)\vec{k}$, m (ft)
$\vec{a}'$	$= (x_1 - x)\vec{i} + \beta(y_1 - y)\vec{j} + \beta(z_1 - z)\vec{k}$, m (ft)
b	span, m (ft)
$\vec{b}$	$= (x_2 - x)\vec{i} + (y_2 - y)\vec{j} + (z_2 - z)\vec{k}$, m (ft)
$\vec{b}'$	$= (x_2 - x)\vec{i} + \beta(y_2 - y)\vec{j} + \beta(z_2 - z)\vec{k}$, m (ft)
C	leading-edge suction parameter (see eq. (41))
$C_{D,i}$	induced-drag coefficient
$C_{D,j}$	drag coefficient due to jet deflection
C_L	total lift coefficient (circulation lift plus jet-reaction lift)
ΔC_L	difference in lift coefficients with jet on and off, except as noted
$C_{L,\Gamma}$	circulation lift coefficient
$C_{l,\Gamma}$	circulation rolling-moment coefficient
C_m	pitching-moment coefficient about Y-axis
$C_{m,\Gamma}$	pitching-moment coefficient about Y-axis due to circulation only

C_T	net thrust coefficient of jet, Net thrust$/q_o S$
C_μ	jet-momentum coefficient, $\dot{m}V_j/q_\infty S$
c	local chord length, m (ft)
$\bar{c}$	reference chord length, m (ft)
$c_{d,i}$	sectional induced-drag coefficient
c_f	flap-chord length, m (ft)
c_{jet}	local chord length at jet center line (see fig. 1), m (ft)
c_ℓ	sectional lift coefficient
$c_{\ell,\Gamma}$	sectional circulation lift coefficient
c_m	sectional pitching-moment coefficient about Y-axis
$c_{m,\Gamma}$	sectional pitching-moment coefficient about Y-axis due to circulation only
c_t	sectional leading-edge thrust coefficient
c_μ	sectional jet-momentum coefficient
D	drag, N (lb)
$\vec{e}$	unit vector tangent to jet path (see fig. 1)
$\vec{G}_\ell$	vector defined by equation (A17)
h_j	distance of jet lower surface to wing surface, m (ft)
$\vec{i},\vec{j},\vec{k}$	unit vectors along X-, Y-, and Z-axes, respectively
L	total lift, N (lb)

$\vec{\ell}$	$= (x_2 - x_1)\vec{i} + (y_2 - y_1)\vec{j} + (z_2 - z_1)\vec{k}$, m (ft)
$\vec{\ell}'$	$= (x_2 - x_1)\vec{i} + \beta(y_2 - y_1)\vec{j} + \beta(z_2 - z_1)\vec{k}$, m (ft)
M	Mach number, or number of integration points
$\vec{M}_\ell$	vector defined by equation (A3) of appendix
$\dot{m}$	mass flow rate, N/sec (slugs/sec)
N	number of chordwise integration points
$[N]$	normal velocity influence-coefficient matrix
$\vec{n}$	unit vector normal to jet surface (see fig. 1)
n, s	jet axis system (see fig. 1)
p	static pressure, N/m^2 (lb/ft^2)
q	dynamic pressure, N/m^2 (lb/ft^2)
$\vec{q}$	induced-velocity vector, m/sec (ft/sec)
R	radius of curvature, m (ft)
$\vec{R}$	$= x\vec{i} + y\vec{j} + z\vec{k}$, m (ft)
R_β^2	$= (x - x')^2 + \beta^2(y - y')^2 + \beta^2(z - z')^2$, m^2 (ft^2)
S	wing area, m^2 (ft^2)
$[S]$	tangential velocity influence-coefficient matrix
s	jet-path coordinate, m (ft)
T	$= \rho_o/\rho_j$
t_j	jet thickness, m (ft)

u	nondimensional perturbed velocity in X-direction
V	velocity
$\vec{V}$	unperturbed velocity vector, m/sec (ft/sec)
$\vec{v}$	perturbed velocity vector, m/sec (ft/sec)
$\vec{v}_{je}$	jet-entrained-flow velocity vector, m/sec (ft/sec)
x,y,z	wing-fixed rectangular coordinates with positive X-axis along axis of symmetry pointing downstream, positive Y-axis pointing to right, and positive Z-axis pointing upward, m (ft)
z_c	coordinate of camber surface, $z_c = z_c(x,y)$, m (ft)
α	angle of attack, deg
β	$= \left(1 - M^2\right)^{1/2}$
γ	nondimensional vortex density, or ratio of specific heats
δ_f	flap deflection, deg
δ_j	jet-deflection angle, deg
θ	angular coordinate (see eq. (A5) of appendix)
$\bar{\theta}(x)$	angle of camber slope
Λ	sweep angle, deg
λ_{12}	reflection coefficient as defined in reference 24
μ	$= V_o/V_j$
μ'	$= \vec{V}_o \cdot \vec{e} / \vec{V}_j \cdot \vec{e}$
w	nondimensional perturbed velocity in Z-direction

ρ	density, kg/m^3 $(slugs/ft^3)$
ϕ	dimensional perturbation velocity potential, m^2/sec (ft^2/sec)
$\overline{\phi}$	nondimensional perturbation velocity potential
ψ	nondimensional additional perturbation velocity potential

Subscripts:

a	additional
e	jet exit
j	jet flow
jj	jet vortices for jet flow
LE	leading edge
o	outer flow
oj	jet vortices for outer flow
TE	trailing edge
w	wing
wa	additional wing vortices
wj	perturbation due to wing in jet flow
wo	perturbation due to wing in outer flow
Γ	circulation
1	first end point of vortex element

2	second end point of vortex element
∞	free stream

MATHEMATICAL FORMULATION

Boundary Conditions

The unperturbed flow, that is, the flow field before the wing is introduced, includes in general the uniform free stream, the jet flow, and the jet-entrained flow due to turbulent mixing. In the following formulation the jet-entrained flow may be regarded as being combined with the uniform free stream to form the outer flow represented by the vector $\vec{V}_o$. As the wing is introduced into the unperturbed flow, perturbations of the jet-flow and the outer-flow fields occur. The calculation of these perturbations represents one of the main problems in the present formulation. The unperturbed jet flow is assumed to be uniform.

These perturbations can be calculated by satisfying the boundary conditions on both the jet and the wing surfaces. The jet boundary conditions require that the jet surface be a stream surface and the pressure be continuous, that is, the pressures on either side of the surface be the same. The stream surface condition is satisfied if the slopes of streamlines on both sides of the jet surface are the same, that is,

$$\frac{\vec{n} \cdot \left(\vec{V}_o + \vec{v}_o\right)}{\vec{e} \cdot \left(\vec{V}_o + \vec{v}_o\right)} = \frac{\vec{n} \cdot \left(\vec{V}_j + \vec{v}_j\right)}{\vec{e} \cdot \left(\vec{V}_j + \vec{v}_j\right)} \tag{1}$$

where $\vec{e}$ is a unit vector tangent to the jet path and $\vec{n}$ is a unit normal vector at the jet surface. (See fig. 1.) The unperturbed jet flow is represented by $\vec{V}_j$ and the perturbations are represented by small letters with appropriate subscripts.

The pressure continuity condition can be formulated (see ref. 15) by using Bernoulli's equation so that

$$p_j\left[1 + \frac{\gamma_j - 1}{2}\frac{\rho_j}{\gamma_j p_j}\left(\left|\vec{V}_j\right|^2 - \left|\vec{V}_j + \vec{v}_j\right|^2\right)\right]^{\frac{\gamma_j}{\gamma_j - 1}} = p_o\left[1 + \frac{\gamma - 1}{2}\frac{\rho_o}{\gamma p_o}\left(\left|\vec{V}_o\right|^2 - \left|\vec{V}_o + \vec{v}_o\right|^2\right)\right]^{\frac{\gamma}{\gamma - 1}} \tag{2}$$

It is assumed that in the unperturbed flow the jet static pressure, p_j, at the jet exit is equal to the pressure of the outer flow, p_o, at the jet exit, so that the static pressures are matched. In addition, if $\gamma_j = \gamma$, equation (2) can be reduced to (see ref. 15)

$$\rho_j\left(\vec{V}_j + \frac{\vec{v}_j}{2}\right) \cdot \vec{v}_j = \rho_o\left(\vec{V}_o + \frac{\vec{v}_o}{2}\right) \cdot \vec{v}_o \tag{3}$$

To simplify equations (1) and (3), it may be assumed that the flow fields are irrotational. Let

$$\vec{v}_j = \left(\vec{V}_o \cdot \vec{n}\right)\vec{n} + \nabla\phi_j \tag{4}$$

$$\vec{v}_o = \nabla\phi_o \tag{5}$$

where $\left(\vec{V}_o \cdot \vec{n}\right)$ is the component of the unperturbed outer flow normal to the jet surface. Introduction of equations (4) and (5) into equation (1) yields

$$\vec{V}_o \cdot \vec{n}(1 - \mu') + \frac{\partial\phi_o}{\partial n} \approx \mu' \frac{\partial\phi_j}{\partial n} \tag{6}$$

assuming that $\vec{e} \cdot \nabla\phi_j \ll \vec{e} \cdot \vec{V}_j$ and $\vec{e} \cdot \nabla\phi_o \ll \vec{e} \cdot \vec{V}_o$ where

$$\left.\begin{aligned} \mu' &= \frac{\vec{V}_o \cdot \vec{e}}{\vec{V}_j \cdot \vec{e}} \\ \vec{V}_j \cdot \vec{n} &= 0 \end{aligned}\right\} \tag{7}$$

Equation (6) is the linearized flow tangency condition at the jet surface. It is seen to be the same as equation (8) of reference 16 in wing-slipstream interaction formulation.

Similarly, a linearized version of the pressure continuity condition is (see ref. 15)

$$\rho_j\left(\vec{V}_j \cdot \vec{e}\right)\frac{\partial\phi_j}{\partial s} \approx \rho_o\left(\vec{V}_o \cdot \vec{e}\right)\frac{\partial\phi_o}{\partial s} \tag{8}$$

where s is the distance measured along the jet path and is taken to be x in the shallow-jet assumption. In deriving equation (8), the quantities $\vec{V}_o \cdot \vec{n}$ and $\vec{V}_j \cdot \vec{n}$ are assumed small.

The wing-flow tangency condition will now be considered. The wing is assumed to be completely in the outer-flow region only. The conventional flow tangency condition is therefore applicable. It follows that on the wing surface the following condition must be satisfied:

$$\frac{\partial\phi_o}{\partial z} = \left(\vec{V}_o \cdot \vec{i}\right)\frac{\partial z_c}{\partial x} - \vec{V}_o \cdot \vec{k} \tag{9}$$

where $z_c(x,y)$ is the wing-camber function.

Method of Flow Singularities

To satisfy the boundary conditions, equations (6), (8), and (9), the method of flow singularities will be used. For this purpose, it is convenient to nondimensionalize the boundary conditions. Let the nondimensional perturbation potentials $\overline{\phi}_o$ and $\overline{\phi}_j$ be defined such that

$$\phi_o = \left(\vec{V}_o \cdot \vec{e}\right)\overline{\phi}_o \tag{10}$$

$$\phi_j = \left(\vec{V}_j \cdot \vec{e}\right)\overline{\phi}_j \tag{11}$$

If it is assumed that $\frac{\partial\left(\vec{V}_o \cdot \vec{e}\right)}{\partial n}$ and $\frac{\partial\left(\vec{V}_o \cdot \vec{e}\right)}{\partial s}$ are small or zero, the boundary conditions, equations (6), (8), and (9), become, respectively,

$$\frac{\partial\overline{\phi}_o}{\partial n} - \frac{\partial\overline{\phi}_j}{\partial n} = -\frac{\vec{V}_o \cdot \vec{n}(1 - \mu')}{\vec{V}_o \cdot \vec{e}} \qquad \text{(On jet surface)} \tag{12}$$

$$\frac{\partial\overline{\phi}_j}{\partial s} - T(\mu')^2\frac{\partial\overline{\phi}_o}{\partial s} = 0 \qquad \text{(On jet surface)} \tag{13}$$

$$\frac{\partial\overline{\phi}_o}{\partial z} = \frac{\vec{V}_o \cdot \vec{i}}{\vec{V}_o \cdot \vec{e}}\frac{\partial z_c}{\partial x} - \frac{\vec{V}_o \cdot \vec{k}}{\vec{V}_o \cdot \vec{e}} \qquad \text{(On wing surface)} \tag{14}$$

where

$$T = \frac{\rho_o}{\rho_j} \tag{15}$$

For numerical convenience, it is advisable to evaluate the wing-alone case separately. For this purpose, it may be noted that in equation (14) $\vec{V}_o \cdot \vec{i} \approx \vec{V}_o \cdot \vec{e}$ in the present linear formulation. Let $\vec{v}_{je}$ be the jet-entrained flow and $\vec{V}_\infty$ the uniform free-stream vector. Then

$$\vec{V}_o = \vec{V}_\infty + \vec{v}_{je} \tag{16}$$

It is assumed that $\vec{V}_o \cdot \vec{e} \approx V_\infty \cos\alpha$.

Two nondimensional potential functions are defined for the wing-alone situation, where there is no jet flow, and are illustrated in the following sketch:

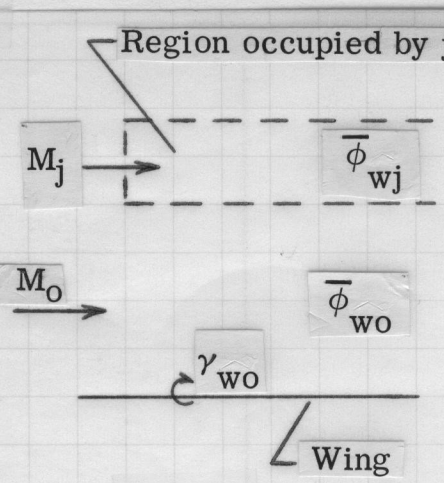

The symbol $\overline{\phi}_{wo}(M_o)$ represents the wing in a uniform free-stream flow having Mach number M_o. The symbol $\overline{\phi}_{wj}(M_j)$ is for the wing in a free-stream flow having Mach number M_j and is defined in that region of the wing's flow field to be occupied by the jet. The presence of the jet is accounted for by the additional perturbation potentials, ψ_o and ψ_j, which are specified for the regions outside and inside the jet. (See the following sketch.)

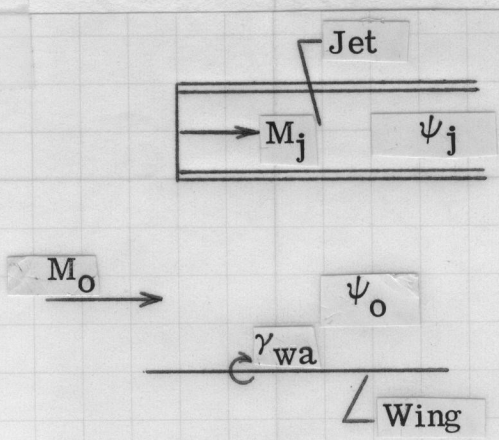

These additional potentials are added to the potentials for the wing-alone flow fields to obtain the total potentials inside and outside of the jet region. Thus,

$$\overline{\phi}_o = \overline{\phi}_{wo}(M_o) + \psi_o(M_o) \tag{17}$$

$$\overline{\phi}_j = \overline{\phi}_{wj}(M_j) + \psi_j(M_j) \tag{18}$$

Using equations (17) and (18) the boundary conditions, equations (12) to (14), become

$$\frac{\partial \psi_o}{\partial n} - \frac{\partial \psi_j}{\partial n} = -\frac{\vec{V}_o \cdot \vec{n}(1 - \mu')}{\vec{V}_o \cdot \vec{e}} + \frac{\partial \overline{\phi}_{wj}}{\partial n}(M_j) - \frac{\partial \overline{\phi}_{wo}}{\partial n}(M_o) \tag{19}$$

$$\frac{\partial \psi_j}{\partial s} - T(\mu')^2 \frac{\partial \psi_o}{\partial s} = -\frac{\partial \bar{\phi}_{wj}}{\partial s} + T(\mu')^2 \frac{\partial \bar{\phi}_{wo}}{\partial s} \tag{20}$$

$$\frac{\partial \psi_o}{\partial z} = -\frac{\vec{v}_{je} \cdot \vec{k}}{V_\infty \cos \alpha} \qquad \text{(On wing surface)} \tag{21}$$

where $\bar{\phi}_{wo}$ and $\bar{\phi}_{wj}$ both satisfy the condition that the flow be tangent to the wing camber surface:

$$\frac{\partial \bar{\phi}_{wo}(M_o)}{\partial z} = \frac{\partial z_c}{\partial x} - \tan \alpha \tag{22a}$$

$$\frac{\partial \bar{\phi}_{wj}(M_j)}{\partial z} = \frac{\partial z_c}{\partial x} - \tan \alpha \tag{22b}$$

The formulation given in equations (19) to (21) is convenient in that, if $\mu' = 1$, $M_o = M_j$, and $\vec{v}_{je} = 0$, then the additional perturbation potentials will be automatically zero.

At this point, a two-vortex-sheet model for the jet surface will be introduced, as illustrated in the following sketch:

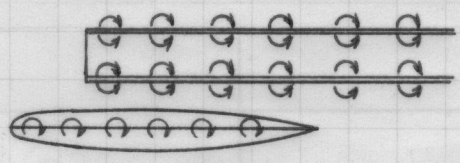

One sheet is to account for the additional perturbation in the outer-flow field and the other for the jet-flow perturbation. This arrangement is required in order to represent the flow field correctly. Any singularity distribution should induce different normal and tangential velocities at all other points on the jet surface depending on whether the surface is approached from inside or outside the jet region, due to Mach number nonuniformity. Ribner and Ellis (ref. 14) introduced a source distribution to account for the jump in normal velocity (eq. (19)). This source distribution would be dependent on the vortex distribution introduced to satisfy equation (20) and vice versa. Hence, additional new integrals for the source distribution must be handled. On the other hand, the present method calls for the use of two vortex sheets so that only vortex integrals must be dealt with.

The resulting vortex integrals are now reduced to finite sums through a quasi-vortex-lattice method (ref. 17). This method represents a refined vortex-lattice method by accounting for the wing-edge singularities and Cauchy singularity in the integrand. It has been found to be more accurate than the conventional vortex-lattice method for a given number of vortex elements used. This property of faster rate of convergence of the method is important in the present formulation in that without it the number of unknown vortex elements would be greatly increased. Now $[S_{JW}]$ may be defined as the s-influence-coefficient matrix for the jet tangential velocities due to the wing; that is,

the matrix elements being the s-perturbed velocities on the jet surface due to unit vortex elements on the wing. Similar definitions are applicable to the matrices $[N_{JW}]$, $[N_{WW}]$, $[N_{WJ}]$, etc., where N denotes the normal components. Using γ with appropriate subscripts to denote the unknown vortex strength, additional perturbed velocities on the jet surface can be written as

$$\left\{\frac{\partial \psi_o}{\partial n}\right\} = [N_{JW}]_{(o)}\{\gamma_{wa}\} + [N_{JJ}]_{(o)}\{\gamma_{oj}\} \tag{23a}$$

$$\left\{\frac{\partial \psi_j}{\partial n}\right\} = [N_{JJ}]_{(j)}\{\gamma_{jj}\} \tag{23b}$$

$$\left\{\frac{\partial \psi_o}{\partial s}\right\} = [S_{JW}]_{(o)}\{\gamma_{wa}\} + [S_{JJ}]_{(o)}\{\gamma_{oj}\} \tag{23c}$$

$$\left\{\frac{\partial \psi_j}{\partial s}\right\} = [S_{JJ}]_{(j)}\{\gamma_{jj}\} \tag{23d}$$

where the subscripts o and j denote the outer and the jet regions, respectively, and $\{\gamma_{wa}\}$ represents the additional wing vortex strengths induced by the jet. Similarly, on the wing surface,

$$\left\{\frac{\partial \psi_o}{\partial z}\right\} = [N_{WW}]\{\gamma_{wa}\} + [N_{WJ}]_{(o)}\{\gamma_{oj}\} \tag{23e}$$

Substitution of equations (23) into equations (19) to (21) gives

$$[N_{JW}]_{(o)}\{\gamma_{wa}\} + [N_{JJ}]_{(o)}\{\gamma_{oj}\} - [N_{JJ}]_{(j)}\{\gamma_{jj}\} = \left\{-\frac{\vec{V}_o \cdot \vec{n}(1-\mu')}{\vec{V}_o \cdot \vec{e}} + \frac{\partial \bar{\phi}_{wj}}{\partial n}(M_j) - \frac{\partial \bar{\phi}_{wo}}{\partial n}(M_o)\right\} \tag{24}$$

$$-T(\mu')^2[S_{JW}]_{(o)}\{\gamma_{wa}\} - T(\mu')^2[S_{JJ}]_{(o)}\{\gamma_{oj}\} + [S_{JJ}]_{(j)}\{\gamma_{jj}\} = \left\{-\frac{\partial \bar{\phi}_{wj}}{\partial s} + T(\mu')^2\frac{\partial \bar{\phi}_{wo}}{\partial s}\right\} \tag{25}$$

and

$$[N_{WW}]\{\gamma_{wa}\} + [N_{WJ}]_{(o)}\{\gamma_{oj}\} = \left\{-\frac{\vec{v}_{je} \cdot \vec{k}}{V_\infty \cos \alpha}\right\} \tag{26}$$

Equations (24) to (26) are written in the form of an augmented matrix equation and are solved by using Purcell's vector method for solving simultaneous equations (ref. 18). The main advantage of this solution technique is that it requires only $\frac{(N_m + 1)^2}{4}$ memory locations for the matrix operation, where N_m is the matrix size.

Once the additional wing vortex strengths, γ_{wa}, have been determined, the total wing γ_w is, then,

$$\gamma_w = \gamma_{wo} + \gamma_{wa} \tag{27}$$

where γ_{wo} is the wing vortex strength in the uniform flow.

Effect of Jet-Sheet Curvature

That part of the jet which is directly on the wing surface is assumed to have no curvature and is therefore independent of the flap deflection. It follows that, if the jet-entrained flow is neglected, the flow tangency condition for the jet becomes

$$-\frac{\vec{V}_o \cdot \vec{n}(1 - \mu')}{\vec{V}_o \cdot \vec{e}} = -(1 - \mu') \tan \alpha \tag{28}$$

The deflected jet sheet behind the trailing edge will be subject to varying angle of attack due to the jet-sheet curvature. This curvature distribution is unknown and is dependent on the unknown jet vortex strength. To avoid iteration, Spence's method in the thin-jet-flap theory (ref. 19) can be adopted here in the following way. Since the jet flow is assumed irrotational, it is true that (see sketch)

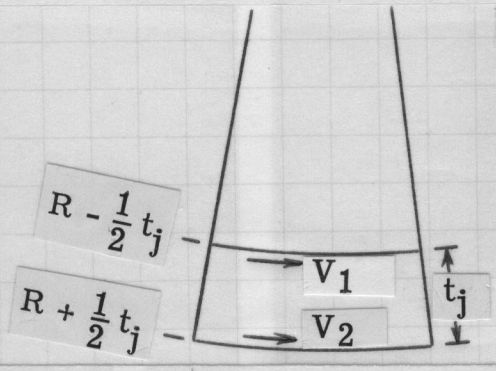

$$V_1\left(R - \tfrac{1}{2} t_j\right) = V_2\left(R + \tfrac{1}{2} t_j\right)$$

or

$$V_1 - V_2 = \frac{V_j t_j}{R} \tag{29}$$

where $V_j = \dfrac{V_1 + V_2}{2}$. The subscripts 1 and 2 used in this section refer to conditions in the jet region on the upper and lower jet surfaces, respectively. Introducing the non-dimensional perturbed velocity potential as given in equation (11), it can be seen that

$$V_1 = V_j + V_j\left(\frac{\partial \bar{\phi}_j}{\partial s}\right)_1$$

$$V_2 = V_j + V_j\left(\frac{\partial \bar{\phi}_j}{\partial s}\right)_2$$

and hence,

$$\left(\frac{\partial \overline{\phi}_j}{\partial s}\right)_1 - \left(\frac{\partial \overline{\phi}_j}{\partial s}\right)_2 = \frac{t_j}{R} \tag{30}$$

Substituting equation (13) into equation (30) yields

$$\frac{t_j}{R} = T(\mu')^2\left[\left(\frac{\partial \overline{\phi}_o}{\partial s}\right)_1 - \left(\frac{\partial \overline{\phi}_o}{\partial s}\right)_2\right]$$

$$= T(\mu')^2\left[\left(\frac{\partial \psi_o}{\partial s}\right)_1 - \left(\frac{\partial \psi_o}{\partial s}\right)_2 + \left(\frac{\partial \overline{\phi}_{wo}}{\partial s}\right)_1 - \left(\frac{\partial \overline{\phi}_{wo}}{\partial s}\right)_2\right] \tag{31}$$

For convenience, let the right-hand side of equation (31) be denoted by $f(x)$:

$$f(x) = T(\mu')^2\left[\left(\frac{\partial \psi_o}{\partial s}\right)_1 - \left(\frac{\partial \psi_o}{\partial s}\right)_2 + \left(\frac{\partial \overline{\phi}_{wo}}{\partial s}\right)_1 - \left(\frac{\partial \overline{\phi}_{wo}}{\partial s}\right)_2\right] \tag{32}$$

For small jet deflection, $\frac{1}{R} \approx \frac{d^2z}{dx^2}$. It follows that the jet path satisfies the following initial-value problem:

$$\left.\begin{aligned} t_j \frac{d^2z}{dx^2} &= f(x) \\ z_{TE} &= 0 \\ \left(\frac{dz}{dx}\right)_{TE} &= -\delta_j \end{aligned}\right\} \tag{33}$$

where δ_j is the jet-deflection angle. Since only the slope $\frac{dz}{dx}$ is needed, complete integration of equations (33) for $z(x)$ is not necessary. To integrate, let

$$x = x_{TE} + \frac{c_j}{2}(1 - \cos\theta) \tag{34}$$

where c_j is the jet length from the wing trailing edge to be included in the analysis. Then equations (33) become

$$t_j \frac{d}{d\theta}\left(\frac{dz}{dx}\right) = \frac{c_j}{2} \sin\theta f(x)$$

Hence,

$$t_j\left(\frac{dz}{dx}\right)_i = -t_j\delta_j + \int_0^{\theta_i} \frac{c_j}{2} \sin\theta f\left[x(\theta)\right] d\theta$$

$$\approx -t_j\delta_j + \frac{\Delta\theta c_j}{2}\left\{\sum_{k=1}^{i-1} \sin\theta_k f\left[x(\theta_k)\right] + \frac{1}{2}\sin\theta_i f\left[x(\theta_i)\right]\right\}$$

where the integral has been reduced to a finite sum through the trapezoidal rule. It follows that at the ith control point on the trailing jet sheet, the jet-path slope is given by

$$\left(\frac{dz}{dx}\right)_i \approx -\delta_j + \frac{\Delta\theta c_j}{2t_j}\left\{\sum_{k=1}^{i-1} \sin\theta_k f\left[x(\theta_k)\right] + \frac{1}{2}\sin\theta_i f\left[x(\theta_i)\right]\right\} \tag{35}$$

Once $\frac{dz}{dx}$ for the jet path is obtained in terms of the unknown vortex strength, the first term on the right-hand side of equation (24) can be written as (again neglecting the jet-entrained flow)

$$-\frac{\vec{V}_o \cdot \vec{n}(1 - \mu')}{\vec{V}_o \cdot \vec{e}} = -\left(-\frac{dz}{dx} + \tan\alpha\right)(1 - \mu') \tag{36}$$

Those terms in $\frac{dz}{dx}$ which depend on the unknown vortex strength are then combined into the left-hand side of equation (24) before the solution is attempted.

Since the s-induced velocities are needed in equation (32), and therefore in the jet-surface tangency condition, equation (24), it is convenient to solve equation (25) first and then equations (24) and (26). This procedure can also avoid the numerical difficulty discussed in reference 15 when some of the jet-control points coincide with some of the wing-control points. The latter would happen if the jet is blowing on the wing surface.

Calculation of Aerodynamic Forces and Moments

To find the sectional aerodynamic characteristics, it is assumed that the wing vortex elements are situated along the actual camber surface. Since the resulting pressure force is normal to the camber surface, the sectional aerodynamic characteristics can be determined by resolving the pressure force in the proper direction and integrating over the local chord. It follows that

$$c_\ell = \frac{2}{\rho_o V_\infty^2 c} \int_0^c \rho_o V_o \left(\vec{V}_o \cdot \vec{e}\right) \gamma_w(x) \cos\left[\alpha - \bar{\theta}(x)\right] dx + c_t \sin\left(\alpha - \bar{\theta}_{LE}\right)$$

$$= \frac{2 \cos \alpha}{c} \int_0^c \gamma_w(x) \cos\left[\alpha - \bar{\theta}(x)\right] dx + c_t \sin\left(\alpha - \bar{\theta}_{LE}\right) \tag{37}$$

$$c_{d,i} = \frac{2 \cos \alpha}{c} \int_0^c \gamma_w(x) \sin\left[\alpha - \bar{\theta}(x)\right] dx - c_t \cos\left(\alpha - \bar{\theta}_{LE}\right) \tag{38}$$

$$c_m \approx \frac{2 \cos \alpha}{\bar{c}c} \int_0^c \gamma_w(x) x \cos\left[\alpha - \bar{\theta}(x)\right] dx \tag{39}$$

where

$$\bar{\theta}(x) = \tan^{-1}\left(\frac{\partial z_c}{\partial x}\right) \tag{40}$$

The integrals in equations (37) to (39) are reduced to finite sums through a modified trapezoidal rule after they are reduced to an integration over an angular coordinate (see ref. 17).

The sectional leading-edge thrust coefficient c_t is computed as (ref. 17)

$$c_t = \frac{\pi}{2} \frac{1}{\cos \Lambda_{LE}} \sqrt{1 - M_o^2 \cos^2 \Lambda_{LE} C^2} \tag{41}$$

where C is the leading-edge suction parameter. According to reference 17 the parameter C can be determined by summing the total induced normal velocity at the leading edge and subtracting the right-hand side of equation (22a) or equation (26), as the case may be. If the induced downwash at the ith leading-edge control point is denoted by a subscript i, then in a manner similar to that used in reference 17, the uniform flow case is

$$NC_1 \sqrt{\tan^2 \Lambda_{LE} + \beta^2} = \left[N_{WW}\right]_i \left\{\gamma_{wo}\right\} - \left\{\frac{\partial z_c}{\partial x} - \tan \alpha\right\}_i \tag{42}$$

Similarly, for the additional flow, it can be shown from equation (26) that

$$NC_2\sqrt{\tan^2 \Lambda_{LE} + \beta^2} = \left[N_{WW}\right]_i \left\langle \gamma_{wa} \right\rangle + \left[N_{WJ}\right]_{(o),i} \left\langle \gamma_{oj} \right\rangle - \left\{ \frac{\vec{v}_{je} \cdot \vec{k}}{V_\infty \cos \alpha} \right\}_i \tag{43}$$

The suction parameter is then $C = C_1 + C_2$.

The overall aerodynamic characteristics of the wing are determined by spanwise integration of the sectional characteristics, as described in reference 17.

The expressions for the elements of the influence-coefficient matrices are described in the appendix.

Numerical Considerations

Since the u-induced velocities, or the $[S]$ matrices, are needed in the present formulation, special care must be exercised in their evaluation. To illustrate this point, consider the expression for $u(x,z)$ for the two-dimensional case in incompressible flow:

$$u(x,z) = \frac{z}{2\pi} \int_0^1 \frac{\gamma(x')\, dx'}{(x - x')^2 + z^2} \tag{44}$$

Observe that for $0 < x < 1$ the integrand in equation (44) has a second-order singularity as z approaches zero while the whole integral is multiplied by z. In fact, it can be shown that $u(x,0) = \frac{\gamma(x)}{2}$. As has been checked numerically, equation (44) can be integrated accurately by the integration technique in the quasi-vortex-lattice method (ref. 17) only if z and the number of integration points are not too small. Increasing the number of integration points, however, would become numerically unrealistic because the number of integration points is equal to the number of unknowns to be solved.

As has been shown in reference 17, the integration technique of the quasi-vortex-lattice method is quite efficient in treating integrals with Cauchy singularity. The best numerical technique under the present circumstances, therefore, is to rewrite equation (44) as

$$\begin{aligned} u(x,z) &= \frac{z}{2\pi} \int_0^1 \frac{\gamma(x') - \gamma(x)}{(x - x')^2 + z^2}\, dx' + \frac{z\gamma(x)}{2\pi} \int_0^1 \frac{dx'}{(x - x')^2 + z^2} \\ &\approx \frac{z}{4\pi} \frac{\pi}{N} \sum_{k=1}^{N} \frac{\gamma(\theta_k) - \gamma(x)}{(x - x_k)^2 + z^2} \sin \theta_k + \frac{z\gamma(x)}{4\pi} \frac{\pi}{M} \sum_{j=1}^{M} \frac{\sin \theta_j}{(x - x_j)^2 + z^2} \end{aligned} \tag{45}$$

where

$$\left.\begin{aligned} \theta_k &= \frac{2k - 1}{2N}\pi \qquad (k = 1, 2, \ldots, N) \\ x_k &= \frac{1}{2}\left(1 - \cos \theta_k\right) \\ \theta_j &= \frac{2j - 1}{2M}\pi \qquad (j = 1, 2, \ldots, M) \\ x_j &= \frac{1}{2}\left(1 - \cos \theta_j\right) \end{aligned}\right\} \tag{46}$$

and M must be chosen so that

$$M = 2^p N \tag{47}$$

for interdigitation between the control and integration points in the last summation and p is an arbitrary integer. This procedure has been found to be quite accurate in most practical applications (ref. 15).

RESULTS AND DISCUSSION

In order to compare the present aerodynamic theory with some available experimental data, it is necessary to account for the reaction forces associated with the jet. The following sketch illustrates the ram drag, $\dot{m}V_\infty$, at the inlet of the nacelle and the jet-reaction force, $\dot{m}V_j$, at the trailing edge of the wing.

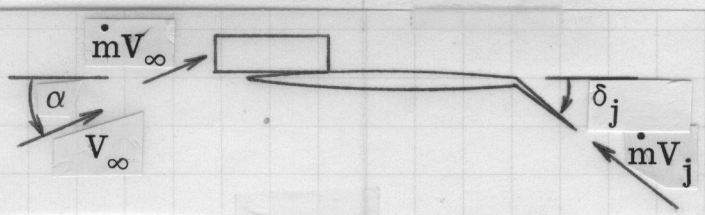

When the flap is deflected, the jet will also deflect due to the viscous interaction between the jet and the flap. Since this effect, commonly referred to as the Coanda effect, can be explained only by viscous-flow theory, its exact prediction is beyond the scope of this study. For the present calculations, therefore, the jet is assumed to deflect with the flap and to preserve its momentum to the trailing edge. This assumption results in a jet-reaction force which is combined with the ram drag to obtain the following jet-deflection forces in the lift and drag directions:

$$L_j = \dot{m}V_j \sin\left(\delta_j + \alpha\right) \tag{48}$$

$$D_j = \dot{m}V_\infty - \dot{m}V_j \cos(\delta_j + \alpha) \tag{49}$$

In the following applications, the jet is assumed to have a constant width, thickness, and velocity, and the jet-entrained flow has been ignored. The lateral expansion of the jet with wind on has been observed experimentally to be relatively limited (refs. 8 and 9). Even if the jet lateral expansion is not ignored in the theoretical model, the increase in lift due to the larger washed area of the lifting surface will be compensated by the associated decrease in the jet dynamic pressure due to enlargement of the jet cross section. A similar situation has been observed experimentally by Seidel (ref. 20) using circular jets with the effect that the wing lift is nearly independent of the horizontal nozzle distance. Similarly, if the jet is allowed to expand vertically, the increase in lift due to larger jet thickness will also be compensated by the associated decrease in the jet dynamic pressure. (See refs. 4 and 21.) It should be emphasized that these are simply assumptions in the present applications of the theory and have not been vigorously verified.

Comparison With Experimental and Theoretical Thin-Jet-Flap Results

There are only limited experimental data for USB configurations available for verification of the present theoretical model. Extensive theoretical and experimental results are available, however, for jet-flap configurations, where it is assumed that a thin jet sheet emanates from the trailing edge. The computer program was slightly modified, therefore, to treat the thin-jet-flap case. According to the thin-jet-flap theory, it is assumed that $\frac{V_j}{V_\infty} \to \infty$ but $V_j^2 t_j$ is finite, where t_j is the jet thickness. It follows that $\mu' = 0$ and the jet flow is unperturbable. This fact implies that $\frac{\partial \overline{\phi}_j}{\partial n} = 0$ in equation (12). In equations (31), (32), and (35), furthermore, the expression $\frac{T(\mu')^2}{t_j}$ can be simplified as

$$\frac{T(\mu')^2}{t_j} = \frac{\rho_\infty V_\infty^2}{\rho_j V_j^2 t_j} = \frac{2}{c_\mu(y)c} \tag{50}$$

where $c_\mu(y) = \frac{\rho_j V_j^2 t_j}{\frac{1}{2}\rho_\infty V_\infty^2 c}$ is the sectional jet-momentum coefficient. To avoid difficulty with the presence of the jet sidewall vortices, the jet thickness was assumed to be 5 percent of the chord length. The trailing jet length to be included in the analysis was determined numerically by using various lengths of the jet sheet until a maximum value for the predicted C_L was reached for a given number of streamwise vortices. From this numerical experimentation, it was found that for practical purposes a jet distance of 2 to 3 chord lengths and 5 to 7 streamwise vortices are sufficient for numerical convergence.

Das' experimental and theoretical section lift and pitching-moment distributions for a wing with half semispan blowing and $\delta_j = 30^o$ (ref. 22) are compared with the present method in figure 2. Experimental and theoretical lift increments due to jet blowing for a rectangular wing with a partial-span flap (ref. 23) are compared with the present method in figure 3. The results by the present theory presented in figure 3 were obtained by adding the predicted incremental lift to the lift at $C_\mu = 0$ given in reference 23. The comparisons in figures 2 and 3 indicate that the predictions of c_ℓ and c_m made with the present method are in good agreement with existing thin-jet-flap theories and experimental data.

Comparison With Thick-Jet Experimental Results

The interaction between a propeller slipstream and a wing is one type of thick-jet problem that has been examined using the present theoretical formulation. This comparison was reported in reference 15, which demonstrated that the current theory provides good agreement with existing theories and experimental data. In order to evaluate the predictive capabilities of the thick-jet-wing interaction theory for USB configurations, the present method is compared with the experimental results of references 4 and 1 in figures 4 and 5, respectively. In order to make these comparisons, the following conditions were imposed:

(a) The jet-deflection angle was assumed to be equal to the flap angle, unless otherwise noted.

(b) The net thrust was assumed to be equal to the experimentally determined static gross thrust.

(c) The jet-exhaust velocity was computed by using the momentum principle which neglects any friction losses, wake rotation, etc. In addition, the jet-exit static pressure was assumed to always be equal to the free-stream static pressure. The momentum theory leads to the following expression which was used to compute velocity as a function of the net thrust coefficient:

$$\frac{V_j}{V_o} = \frac{1}{2}\left\{1 + \left[1 + \frac{2C_T(S/2)}{A_j(\rho_j/\rho_o)}\right]^{1/2}\right\} \tag{51}$$

where A_j is the jet cross-sectional area. (Note that C_T is the total thrust for two engines.)

According to the experimental observations of references 4 and 9, the jet is deflected even though the flap is undeflected, mainly due to the curvature of the upper surface of the airfoil. The trailing-edge angle of the airfoil's upper surface was quoted in reference 4 to be 12^o; this was also the jet-deflection angle assumed in the present computation. The

configuration which has twist and camber is idealized as shown in figure 4(a). The theoretical results at two C_T's compared with the measurements and thin-jet-flap results are illustrated in figure 4(b). The experimental results are given in figure 36 of reference 4. The theoretical curves are obtained by adding the predicted lift increments at each α to the experimental wing-alone results. The present method slightly overpredicted the lift at $C_T = 2.0$ and underpredicted it at $C_T = 0.5$. It is seen that the thin-jet-flap theory underpredicted the lift for $C_T = 2.0$.

Since in the experimental data the thrust and scrubbing drag have all been included in the total drag, it is not possible to compare the induced-drag prediction alone. The following method can be used to check the theory indirectly, however. If it is assumed that the scrubbing drag is independent of α, then the following drag increment,

$$\Delta C_{D_{(\alpha)}} = C_{D_{(\alpha)}} - C_{D_{(\alpha=1^\circ)}} \tag{52}$$

can be regarded as due to the induced drag and the jet-reaction effect. The induced drag is directly computed in the program and the jet-reaction effect is estimated by equation (49). The drag increment due to angle of attack, therefore, is estimated by the present theory using the following relation:

$$\Delta C_{D_{(\alpha)}} = \left(C_{D,i} + C_{D,j}\right)_{(\alpha)} - \left(C_{D,i} + C_{D,j}\right)_{(\alpha=1^\circ)} \tag{53}$$

Using this procedure, the drag increment is obtained at $\alpha = 6^\circ$ and 11° and is compared in table 1. It is seen that the agreement is reasonable.

TABLE 1.- COMPARISON OF PREDICTED INDUCED DRAG INCREMENTS AT ANGLES OF ATTACK WITH MEASUREMENTS FROM REFERENCE 4

α, deg	$\Delta C_{D(\alpha)}$			
	$C_T = 0.5$		$C_T = 2.0$	
	Theory	Experiment	Theory	Experiment
6	0.043	≈0	0.112	0.15
11	.114	.1	.29	.3

The second test case is a configuration with full-span flap deflection of 30°, as given in reference 1. The idealized planform is illustrated in figure 5(a), where the body cutout, the leading-edge Krueger flap, and the trailing-edge flap extension have been ignored, and the jet-exit location was at 0.23 of the local chord. The lift-coefficient against angle-of-attack curves are compared in figure 5(b), where the theoretical curve

is obtained by adding the predicted lift increments to the experimental curve for power off. As with the first test case, the prediction of C_L is reasonably good.

Configuration and Jet-Parameter Effects

Effects of jet-exit longitudinal location.- The effects of moving the jet exit in the chordwise direction are illustrated in figure 6 for the configuration of figure 5(a). The figure shows the jet-induced lift generated by the jet, which is located at chord stations from the leading edge to the trailing edge, for three angles of attack. The results indicate that moving the jet exit forward from the trailing edge is beneficial for lift augmentation and that the largest lift augmentations occur with the jet exit located at, or forward of, the leading edge.

Jet-thickness effects at constant C_T and jet span.- For all of the following calculations, the transport-type planform shown in figure 7 will be used, unless otherwise noted. Assuming a flat-plate airfoil and $C_T = 0.2$, to simulate a cruise condition, three sets of theoretical curves have been plotted in figure 8 to demonstrate the effects of jet thickness. The first and second curves allow the jet Mach number to vary according to

$$M_j = M_o\left(\frac{V_j}{V_o}\right)\left(\frac{\rho_j}{\rho_o}\right)^{1/2} \tag{54}$$

It follows from equation (51) that, as the jet thickness is reduced with C_T constant and the jet width is fixed, the jet velocity and the jet Mach number would be increased. The third curve was obtained by taking $M_o = M_j = 0.3$ and $\rho_o = \rho_j$. This assumption neglects the interaction process that takes place when the Mach numbers are different. The following observations can be made about the results shown in figure 8:

(a) With the Mach number interaction between the streams neglected $(M_j = M_o)$, the third curve shows that a jet thickness exists which yields maximum lift and induced drag. This result is due to the fact that the effects of jet thickness and jet velocity are compensating. In other words, the thinner jet reduces the lift while the higher jet velocity increases the lift. With the jet thickness reduced to zero, power-off results would be produced independent of the jet-velocity ratio, as has been shown in reference 24 for the two-dimensional case.

(b) When the jet Mach number is allowed to vary, as was done for the first and second curves, M_j soon becomes too high as the thickness is reduced, that is, $M_j \geq 1$, for the linear subsonic theory to be valid. Therefore, the computation has not been carried out to find the thickness for the maximum lift and induced drag.

(c) Accounting for Mach number differences resulted in increases in lift and induced drag with increases in M_j, which can be seen by comparing curves 1 and 3. This result can be explained by the reflection coefficient defined in reference 24:

$$\lambda_{12} = -\frac{\frac{\rho_j V_j^2}{\rho_o V_o^2} - \frac{\beta_j}{\beta_o}}{\frac{\rho_j V_j^2}{\rho_o V_o^2} + \frac{\beta_j}{\beta_o}} \tag{55}$$

where $\beta = \sqrt{1 - M^2}$. Reference 24 showed that a more negative reflection coefficient will result in higher lift, and an increase in M_j tends to change λ_{12} negatively.

Effect of jet temperature.- The effect of jet temperature can be observed in figure 8 by comparing curves 1 and 2 (solid and dashed lines) and noting that the density ratio (ρ_o/ρ_j) is equal to the ratio of the jet to the free-stream temperature, for the case where $p_o = p_j$. Increasing jet temperature tends to decrease the lift and induced drag, primarily because this increase would reduce the jet dynamic pressure. To see this effect, the ratio of free stream to jet dynamic pressures, $T\mu^2$, for small values of α can be reduced to

$$T\mu^2 = \frac{\rho_o V_o^2}{\rho_j V_j^2} = \frac{4T}{\left[1 + \sqrt{1 + \frac{2C_T \frac{S}{2} T}{A_j}}\right]^2}$$

$$= \frac{2T}{1 + \frac{C_T \frac{S}{2} T}{A_j} + \sqrt{1 + \frac{2C_T \frac{S}{2} T}{A_j}}}$$

$$= \frac{2}{\frac{1}{T} + \frac{C_T \frac{S}{2}}{A_j} + \sqrt{\frac{1}{T^2} + \frac{2C_T \frac{S}{2}}{A_j T}}} \tag{56}$$

where equation (51) has been used. Equation (56) shows that $T\mu^2$ increases as $T\left(= \frac{\rho_o}{\rho_j}\right)$ increases. Increasing T_j would also affect M_j, but this would be a secondary effect compared to the dynamic pressure change. It is recalled that, for the present development, the ratio of specific heats in the jet is assumed equal to that in the outer flow and thus is not a function of T_j.

The lift reduction due to hot jet at a constant C_T has been measured experimentally (ref. 8).

Effects of jet aspect ratio.- The jet aspect ratio is defined as the ratio of jet width to jet thickness. To investigate the effect of AR_j, the jet center line is assumed fixed $\left(\frac{2y}{b} = 0.282\right)$ and the jet span and the thickness are changed in such a way that the jet cross-sectional area is unchanged. The results at $C_T = 0.2$ are plotted in figure 9 for $AR_j = 6.825$ and 3.033. The jet-deflection angle was 10^o. These results tend to confirm the results of reference 10 which show that higher AR_j will produce higher $C_{L,\Gamma}$ and $C_{D,i}$ at a given α, where $C_{L,\Gamma}$ is the circulation lift coefficient. From the $C_{L,\Gamma}$ against $C_{D,i}$ curve, however, the performance of the wing with either of these two jet nozzles is seen to be approximately the same. It should be remembered that higher AR_j jet would yield higher scrubbing drag.

Effects of jet deflection on cruise performance.- Again, the same cambered wing as used previously was employed with the jet exit either at 0.25c or at the leading edge. As shown in figure 10, the jet-deflection effect is seen to be beneficial and the jet exit should be as close to the leading edge as possible. For the latter case, the jet will enhance the loading near the leading edge to produce higher leading-edge thrust. It will also produce a force component in the thrust direction due to the pressure loading at small α because of the positive camber slope there. At high α, this latter benefit disappears so that the jet tends to produce more induced drag than the power-off case. Since the jet-deflection effect is favorable on cruise performance, a thick wing which has high upper-surface slope at the trailing edge may be preferable to a thin wing from the aerodynamic point of view.

Effects of jet interaction on the aerodynamic center.- At small values of C_T, the effect of power on the aerodynamic center is small, as has been found from the computations at $C_T = 0.2$. To determine the effect at high values of C_T, the configuration shown in figure 7 is again used, with the flap-chord ratio of 0.3, full-span flap deflection of 30^o, and the jet exit at the leading edge. The aerodynamic center (a.c.) was computed by finding the ratio, $-\Delta C_m/\Delta C_L$, with ΔC_m and ΔC_L calculated between $\alpha = 1^o$ and 5^o. The jet-reaction effect is not included. As shown in figure 11, increasing jet thrust moves the a.c. forward, where the a.c. is expressed in terms of fraction of the root chord and is measured from the wing vertex. This conclusion is consistent with the experimental results (ref. 1) where the a.c. shift as high as 10 percent of the mean aerodynamic chord has been reported. Since the a.c. is affected by the jet-deflection effect, which varies with the flap angle, it follows that the a.c. shift must also be a function of flap angle. This effect is illustrated in figure 12 for $C_T = 2.0$, where Δa.c. represents the shift in a.c. location between power on and power off and is shown plotted with respect to δ_j. The a.c. is shifted forward when the jet-deflection angle is increased.

Effects of vertical shift of jet location.- The effect of jet vertical location on the aerodynamic characteristics is shown in figure 13, where the jet lower surface is taken to be on the upper surface of the wing and then is shifted upward one-half of a jet thickness.

It is assumed that the jet-deflection effect is completely lost once the jet is shifted away from the wing surface. It is seen that at a given circulation lift the wing with the vertically shifted jet would have higher induced drag. This result is mainly due to the high rate of lift reduction associated with this vertical shift.

To show how fast the aerodynamic characteristics would change as the jet is shifted upwards, the configuration of figure 5(a) without flap deflection and with the jet exit at the leading edge was used. With $C_T = 2.095$ at $\alpha = 5^o$, the results of figure 14 show the rapid changes in ΔC_L and $\Delta C_{D,i}$ which are the net changes with respect to the wing-alone case.

Figure 15 illustrates the effect jet vertical location has on span loading, where the left engine is inoperative. Shifting the jet vertically results in significant reductions in $C_{l,\Gamma}$, which leads to corresponding reductions in rolling-moment coefficient. Of course, the lift coefficient is also reduced.

Effects of wing aspect ratio on lift capability.- The effects on lift augmentation of changing wing aspect ratio from 8 to 4 are shown in figure 16 for a rectangular-wing planform. The aspect ratio is changed by varying the wing span with fixed chord length and jet geometry. The area of the wing with $AR = 8$ is used in computing C_L for all wings. The results were obtained at $\alpha = 5^o$ and $\delta_f = 30^o$ $\left(\frac{c_f}{c} = 0.3\right)$ with the jet exit located at the leading edge. The results show that the reduction in circulation lift when the aspect ratio is reduced from 8 to 4 is 24 percent at $C_T = 2.0$.

An analogous situation exists in reference 21 for a thin jet blowing at the trailing edge of a rectangular wing. For this case, the circulation lift for a wing of $AR = 4.15$ with full-span blowing is about 31 percent less than that for a wing of $AR = 8.3$ with inboard half-span blowing.

CONCLUDING REMARKS

A theoretical method has been formulated which accounts for the wing-jet interaction and Mach number nonuniformity for the USB configurations. The theoretical results were in good agreement with experimental lift, induced-drag, and pitching-moment data for configurations with thin and thick jet exhausts.

Additional theoretical results showed that (1) the lift and induced drag are reduced by increasing jet temperature and are increased by increasing jet Mach number; (2) reducing jet aspect ratio with a constant jet cross-sectional area reduces the lift, induced drag, and pitching moment at a given angle of attack but with a minimal change in the induced drag polar curve; (3) the jet-deflection effect is beneficial at cruise and therefore a thick wing is preferable to a thin wing because of the greater upper-surface slope at the wing's trailing edge; (4) the aerodynamic center is shifted forward by power and/or jet-deflection

angle; (5) moving the jet away from the wing surface will change the lift and induced drag rapidly; and (6) reducing the wing span of a rectangular wing by half decreases the jet-circulation lift by only 24 percent at a jet thrust coefficient of 2.0.

Langley Research Center
National Aeronautics and Space Administration
Hampton, Va. 23665
June 9, 1975

APPENDIX

EXPRESSIONS FOR INFLUENCE-COEFFICIENT MATRICES

For the purpose of satisfying the boundary conditions, the continuous wing and jet vortex sheets are replaced by stepwise constant vortex distributions in the spanwise direction. The induced velocity vector due to a "bounded" vortex element of strength $\gamma\, dx'$ can be shown to be (ref. 17)

$$d\vec{q}_1(\vec{R}) = \frac{\beta^2 \gamma\, dx'}{4\pi} \frac{\vec{a} \times \vec{\ell}}{\left|\vec{a}' \times \vec{\ell}'\right|^2} \left\{ \frac{\vec{b}'}{\left|\vec{b}'\right|} - \frac{\vec{a}'}{\left|\vec{a}'\right|} \right\} \cdot \vec{\ell}' \tag{A1}$$

where

$$\left.\begin{aligned}
\vec{a} &= (x_1 - x)\vec{i} + (y_1 - y)\vec{j} + (z_1 - z)\vec{k} \\
\vec{b} &= (x_2 - x)\vec{i} + (y_2 - y)\vec{j} + (z_2 - z)\vec{k} \\
\vec{a}' &= (x_1 - x)\vec{i} + \beta(y_1 - y)\vec{j} + \beta(z_1 - z)\vec{k} \\
\vec{b}' &= (x_2 - x)\vec{i} + \beta(y_2 - y)\vec{j} + \beta(z_2 - z)\vec{k} \\
\vec{\ell} &= (x_2 - x_1)\vec{i} + (y_2 - y_1)\vec{j} + (z_2 - z_1)\vec{k} \\
\vec{\ell}' &= (x_2 - x_1)\vec{i} + \beta(y_2 - y_1)\vec{j} + \beta(z_2 - z_1)\vec{k} \\
\vec{R} &= x\vec{i} + y\vec{j} + z\vec{k}
\end{aligned}\right\} \tag{A2}$$

The geometry is illustrated in the following sketch:

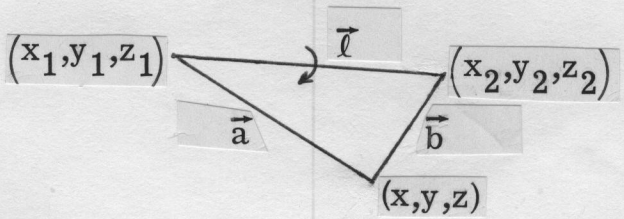

For simplicity, define

$$\vec{M}_\ell(x',\vec{R}) = \frac{\vec{a} \times \vec{\ell}}{\left|\vec{a}' \times \vec{\ell}'\right|^2} \left\{ \frac{\vec{b}'}{\left|\vec{b}'\right|} - \frac{\vec{a}'}{\left|\vec{a}'\right|} \right\} \cdot \vec{\ell}' \tag{A3}$$

Integrating equation (A1) over a vortex strip gives

$$\vec{q}_1\left(\vec{R}\right) = \frac{\beta^2}{4\pi}\int_{x_\ell}^{x_t} \gamma(x')\vec{M}_\ell\left(x',\vec{R}\right)\,dx' \tag{A4}$$

where x_t and x_ℓ are the end points of the vortex strip. Using the following transformation

$$x' = x_\ell + \frac{1}{2}(x_t - x_\ell)(1 - \cos\theta) \tag{A5}$$

equation (A4) becomes

$$\vec{q}_1\left(\vec{R}_i\right) = \frac{\beta^2(x_t - x_\ell)}{8\pi}\int_0^\pi \gamma(\theta)\vec{M}_\ell\left(\theta,\vec{R}_i\right)\sin\theta\,d\theta$$

$$\approx \frac{\beta^2(x_t - x_\ell)}{8\pi}\frac{\pi}{N}\sum_{k=1}^{N}\gamma\left(\theta_k\right)\vec{M}_\ell\left(\theta_k,\vec{R}_i\right)\sin\theta_k \tag{A6}$$

where the midpoint modified trapezoidal rule has been used to reduce the integral to a finite sum (ref. 17) and

$$\theta_k = \frac{2k - 1}{2N}\pi \qquad (k = 1, 2, \ldots, N) \tag{A7}$$

$$x_i = x_\ell + \frac{1}{2}(x_t - x_\ell)\left(1 - \cos\frac{i\pi}{N}\right) \qquad (i = 1, 2, \ldots, N) \tag{A8}$$

In addition, the induced velocity due to the associated trailing vortices from end point 2 can be written as

$$\vec{q}_{2(2)}\left(\vec{R}\right) = \frac{\beta^2}{4\pi}\int \gamma(x')\,dx' \int_{x'}^{\infty}\frac{\left(\vec{R}' - \vec{R}\right)x\,d\vec{\ell}_2}{R_\beta^3} \tag{A9}$$

where

$$\vec{R}' - \vec{R} = (x' - x)\vec{i} + (y' - y)\vec{j} + (z' - z)\vec{k} \tag{A10}$$

$$R_\beta^2 = (x - x')^2 + \beta^2(y - y')^2 + \beta^2(z - z')^2 \tag{A11}$$

$$d\vec{\ell}_2 = dx'_2\vec{i} + dy'_2\vec{j} + dz'_2\vec{k} \tag{A12}$$

Define

$$\vec{G}_{\ell_{(2)}}(x',\vec{R}) = \int_{x'}^{\infty} \frac{(\vec{R}' - \vec{R}) \times d\vec{\ell}_2}{R_\beta^3} \tag{A13}$$

For trailing vortices which are assumed to trail back on the wing plane, $\vec{G}_{\ell_{(2)}}$ can be shown to be (ref. 15)

$$\vec{G}_{\ell_{(2)}} = \vec{j}\frac{z_2 - z}{\beta^2\left[(y - y_2)^2 + (z - z_2)^2\right]}\left\{1 - \frac{x_2 - x}{\left[(x - x_2)^2 + \beta^2(y - y_2)^2 + \beta^2(z - z_2)^2\right]^{1/2}}\right\}$$

$$- \vec{k}\frac{y_2 - y}{\beta^2\left[(y - y_2)^2 + (z - z_2)^2\right]}\left\{1 - \frac{x_2 - x}{\left[(x - x_2)^2 + \beta^2(y - y_2)^2 + \beta^2(z - z_2)^2\right]^{1/2}}\right\} \tag{A14}$$

Similarly, for trailing vortices emanating from end point 1, the induced velocity is given by (noting that $d\vec{\ell}_1 = -d\vec{\ell}_2$)

$$\vec{q}_{2_{(1)}}(\vec{R}) = \frac{\beta^2}{4\pi}\int_{x_\ell}^{x_t} \gamma(x')\, dx'\, \vec{G}_{\ell_{(1)}}(x',\vec{R}) \tag{A15}$$

where

$$\vec{G}_{\ell_{(1)}}(x',\vec{R}) = \int_{x'}^{\infty} \frac{(\vec{R}' - \vec{R}) \times d\vec{\ell}_1}{R_\beta^3}$$

$$= -\vec{j}\frac{z_1 - z}{\beta^2\left[(y - y_1)^2 + (z - z_1)^2\right]}\left\{1 - \frac{x_1 - x}{\left[(x - x_1)^2 + \beta^2(y - y_1)^2 + \beta^2(z - z_1)^2\right]^{1/2}}\right\}$$

$$+ \vec{k}\frac{y_1 - y}{\beta^2\left[(y - y_1)^2 + (z - z_1)^2\right]}\left\{1 - \frac{x_1 - x}{\left[(x - x_1)^2 + \beta^2(y - y_1)^2 + \beta^2(z - z_1)^2\right]^{1/2}}\right\} \tag{A16}$$

Let

$$\vec{G}_\ell(x',\vec{R}) = \vec{G}_{\ell_{(1)}}(x',\vec{R}) + \vec{G}_{\ell_{(2)}}(x',\vec{R}) \tag{A17}$$

Then the induced velocity due to the trailing vortices from both end points is

$$\vec{q}_2(\vec{R}) = \frac{\beta^2}{4\pi}\int_{x_\ell}^{x_t} \gamma(x')\vec{G}_\ell(x',\vec{R})\,dx' \tag{A18}$$

Again, applying the transformation of equation (A5) to equation (A18)

$$\vec{q}_2(\vec{R}_i) \approx \frac{\beta^2(x_t - x_\ell)}{8\pi}\frac{\pi}{N}\sum_{k=1}^{N}\gamma(\theta_k)\vec{G}_\ell(\theta_k,\vec{R}_i)\sin\theta_k \tag{A19}$$

is obtained. The total induced velocity, $\vec{v}_\theta$, at a control point i due to a vortex strip is, therefore, the sum of $\vec{q}_1$ and $\vec{q}_2$:

$$\vec{v}_\theta(\vec{R}_i) \approx \frac{\beta^2(x_t - x_\ell)}{8N}\sum_{k=1}^{N}\gamma_k \sin\theta_k\left[\vec{M}_\ell(\theta_k,\vec{R}_i) + \vec{G}_\ell(\theta_k,\vec{R}_i)\right] \tag{A20}$$

It follows that the normal velocity induced at i due to a unit vortex strength at k, or the (i,k) element of the influence-coefficient matrix $[N]$, can be written as

$$N_{ik} = \frac{\beta^2(x_t - x_\ell)}{8N}\sin\theta_k\left[\vec{M}_\ell(\theta_k,\vec{R}_i)\cdot\vec{n}_i + \vec{G}_\ell(\theta_k,\vec{R}_i)\cdot\vec{n}_i\right] \tag{A21}$$

For the case where the unit normal vector $\vec{n} = \vec{k}$, it can be easily shown that

$$\vec{M}_\ell(\theta_k,\vec{R}_i)\cdot\vec{n}_i = \frac{(x_1 - x_i)(y_2 - y_1) - (y_1 - y_i)(x_2 - x_1)}{\left|\vec{a}'\times\vec{\ell}'\right|_i^2}\left\{\frac{\vec{b}'\cdot\vec{\ell}'}{|\vec{b}'|} - \frac{\vec{a}'\cdot\vec{\ell}'}{|\vec{a}'|}\right\}_i \tag{A22}$$

and

$$\vec{G}_\ell(\theta_k,\vec{R}_i)\cdot\vec{n}_i = -\frac{y_2 - y}{\beta^2\left[(y_i - y_2)^2 + (z_i - z_2)^2\right]}\left\{1 - \frac{x_2 - x_i}{\left[(x_i - x_2)^2 + \beta^2(y_i - y_2)^2 + \beta^2(z_i - z_2)^2\right]^{1/2}}\right\}$$

$$+\frac{y_1 - y}{\beta^2\left[(y_i - y_1)^2 + (z_i - z_1)^2\right]}\left\{1 - \frac{x_1 - x_i}{\left[(x_i - x_1)^2 + \beta^2(y_i - y_1)^2 + \beta^2(z_i - z_1)^2\right]^{1/2}}\right\} \tag{A23}$$

Similarly, the (i,k) element of the matrix $[S]$ can be written as

$$S_{ik} = \frac{\beta^2(x_t - x_\ell)}{8N} \sin\theta_k \left[\vec{M}_\ell\left(\theta_k, \vec{R}_i\right) \cdot \vec{e}_i + \vec{G}_\ell\left(\theta_k, \vec{R}_i\right) \cdot \vec{e}_i\right] \tag{A24}$$

For $\vec{e}_i = \vec{i}$, as being assumed in the present applications, it is known that

$$\vec{G}_\ell \cdot \vec{i} = 0 \tag{A25}$$

and

$$\vec{M}_\ell \cdot \vec{e}_i = \frac{(y_1 - y_i)(z_2 - z_1) - (z_1 - z_i)(y_2 - y_1)}{\left|\vec{a}' \times \vec{\ell}'\right|_i^2} \left\{\frac{\vec{b}' \cdot \vec{\ell}'}{\left|\vec{b}'\right|} - \frac{\vec{a}' \cdot \vec{\ell}'}{\left|\vec{a}'\right|}\right\}_i \tag{A26}$$

On the jet side panels, $\vec{n}$ would be $\vec{j}$ on the outboard panels and $-\vec{j}$ on the inboard panels. It follows that

$$\vec{M}_\ell \cdot \vec{n}_i = \mp \frac{(x_1 - x_i)(z_2 - z_1) - (z_1 - z_i)(x_2 - x_1)}{\left|\vec{a}' \times \vec{\ell}'\right|_i^2} \left\{\frac{\vec{b}' \cdot \vec{\ell}'}{\left|\vec{b}'\right|} - \frac{\vec{a}' \cdot \vec{\ell}'}{\left|\vec{a}'\right|}\right\}_i \tag{A27}$$

and

$$\vec{G}_\ell \cdot \vec{n}_i = \pm \frac{z_2 - z_i}{\beta^2\left[(y_i - y_2)^2 + (z_i - z_2)^2\right]} \left\{1 - \frac{x_2 - x_i}{\left[(x_i - x_2)^2 + \beta^2(y_i - y_2)^2 + \beta^2(z_i - z_2)^2\right]^{1/2}}\right\}$$

$$\mp \frac{z_1 - z_i}{\beta^2\left[(y_i - y_1)^2 + (z_i - z_1)^2\right]} \left\{1 - \frac{x_1 - x_i}{\left[(x_i - x_1)^2 + \beta^2(y_i - y_1)^2 + \beta^2(z_i - z_1)^2\right]^{1/2}}\right\} \tag{A28}$$

where the upper sign is for the outboard side panel. Equations (A25) and (A26) are still valid for this case.

REFERENCES

1. Phelps, Arthur E.; Letko, William; and Henderson, Robert L.: Low-Speed Wind-Tunnel Investigation of a Semispan STOL Jet Transport Wing-Body With an Upper-Surface Blown Jet Flap. NASA TN D-7183, 1973.

2. Aoyagi, Kiyoshi; Falarski, Michael D.; and Koenig, David G.: Wind Tunnel Investigation of a Large-Scale Upper Surface Blown-Flap Transport Model Having Two Engines. NASA TM X-62,296, 1973.

3. Phelps, Arthur E., III; and Smith, Charles C., Jr.: Wind-Tunnel Investigation of an Upper Surface Blown Jet-Flap Powered-Lift Configuration. NASA TN D-7399, 1973.

4. Smith, Charles C., Jr.; Phelps, Arthur E., III; and Copeland, W. Latham: Wind-Tunnel Investigation of a Large-Scale Semispan Model With an Unswept Wing and an Upper-Surface Blown Jet Flap. NASA TN D-7526, 1974.

5. Shivers, James P.; and Smith, Charles C., Jr.: Preliminary Static Tests of a Simulated Upper-Surface Blown Jet-Flap Configuration Utilizing a Full-Size Turbofan Engine. NASA TM X-71931, 1974.

6. Smith, Charles C., Jr.; and White, Lucy C.: Pressure Distribution of a Twin-Engine Upper-Surface Blown Jet-Flap Model. NASA TM X-71937, 1974.

7. Parlett, Lysle P.: Free-Flight Wind-Tunnel Investigation of a Four-Engine Sweptwing Upper-Surface Blown Transport Configuration. NASA TM X-71932, 1974.

8. Johnson, Joseph L., Jr.; and Phelps, Arthur E., III: Low-Speed Aerodynamics of the Upper-Surface Blown Jet Flap. [Preprint] 740470, Soc. Automot. Eng., Apr.-May 1974.

9. Wimpress, John K.: Upper Surface Blowing Technology as Applied to the YC-14 Airplane. [Preprint] 730916, Soc. Automot. Eng., Oct. 1973.

10. Skavdahl, Howard; Wang, Timothy; and Hirt, William J.: Nozzle Development for the Upper Surface – Blown Jet Flap on the YC-14 Airplane. [Preprint] 740469, Soc. Automot. Eng., Apr.-May 1974.

11. Lopez, M. L.; and Shen, C. C.: Recent Developments in Jet Flap Theory and Its Application to STOL Aerodynamic Analysis. AIAA Paper No. 71-578, 1971.

12. Turner, Thomas R.; Davenport, Edwin E.; and Riebe, John M.: Low-Speed Investigation of Blowing From Nacelles Mounted Inboard and on the Upper Surface of an Aspect-Ratio-7.0 35^{o} Swept Wing With Fuselage and Various Tail Arrangements. NASA MEMO 5-1-59L, 1959.

13. Küchemann, Dietrich; and Weber, Johanna: Aerodynamics of Propulsion. McGraw-Hill Book Co., Inc., 1953.

14. Ribner, H. S.; and Ellis, N. D.: Aerodynamics of Wing-Slipstream Interaction. C.A.S.I. Trans., vol. 5, no. 2, Sept. 1972, pp. 56-63.

15. Lan, C. Edward: An Analytical Investigation of Wing-Jet Interaction. CRINC-FRL 74-001 (NASA Grant NGR 17-002-107), Univ. of Kansas, Apr. 1974. (Available as NASA CR-138140.)

16. Levinsky, E. S.; Thommen, H. U.; Yager, P. M.; and Holland, C. H.: Lifting-Surface Theory for V/STOL Aircraft in Transition and Cruise. I. J. Aircraft, vol. 6, no. 6, Nov.-Dec. 1969, pp. 488-495.

17. Lan, C. Edward: A Quasi-Vortex-Lattice Method in Thin Wing Theory. J. Aircraft, vol. 11, no. 9, Sept. 1974, pp. 518-527.

18. Purcell, Everett W.: The Vector Method of Solving Simultaneous Linear Equations. J. Math. & Phys., vol. 32, no. 2-3, July-Oct. 1953, pp. 180-183.

19. Spence, D. A.: The Lift Coefficient of a Thin, Jet-Flapped Wing. Proc. Roy. Soc. (London), ser. A, vol. 238, no. 1212, Dec. 4, 1956, pp. 46-68.

20. Seidel, M.: The Influence of an Inclined Jet on the Flow Field in the Vicinity of a Lifting Surface and on Its Aerodynamic Coefficients. NASA TT F-14,956, 1973.

21. Gainer, Thomas G.: Low-Speed Wind-Tunnel Investigation To Determine the Aerodynamic Characteristics of a Rectangular Wing Equipped With a Full-Span and an Inboard Half-Span Jet-Augmented Flap Deflected 55°. NASA MEMO 1-27-59L, 1959.

22. Das, Arabino: Theoretische und experimentelle Untersuchungen an Tragflügeln endlicher Spannweite mit Strahlklappen. Abh. Braunschw. Wiss. Ges., Bd. XVII, 1965, pp. 21-50.

23. Williams, J.; Butler, S. F. J.; and Wood, M. N.: The Aerodynamics of Jet Flaps. R. & M. No. 3304, British A.R.C., 1963.

24. Lan, C. Edward: Some Characteristics of Airfoil-Jet Interaction With Mach Number Nonuniformity. J. Aircraft, vol. 11, no. 8, Aug. 1974, pp. 491-494.

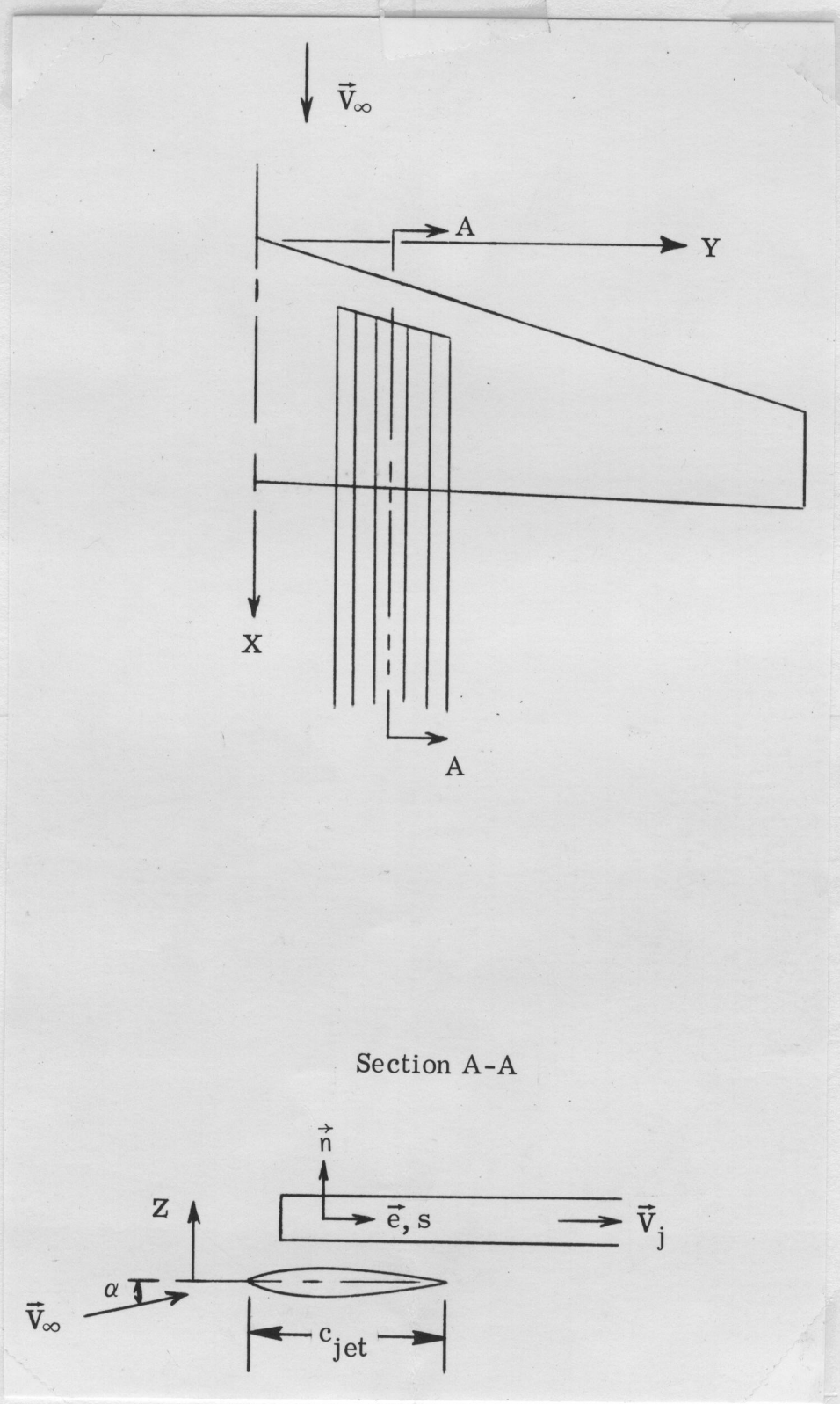

Figure 1.- Schematic of wing and jet.

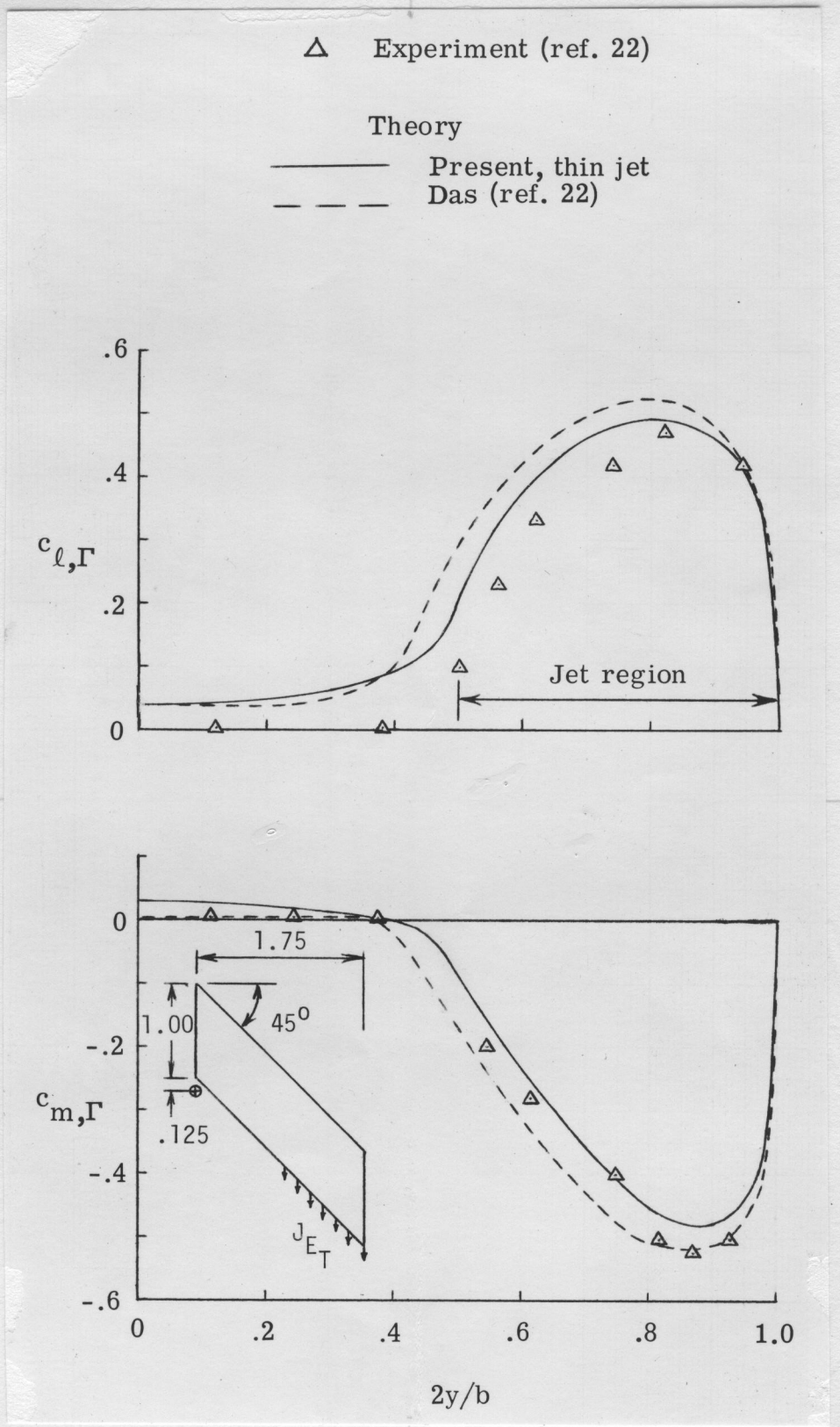

Figure 2.- Comparison of predicted section characteristics with experiment for the thin-jet configuration of reference 22. $\alpha = 0^{o}$, $\delta_j = 30^{o}$, $M_o = 0$, $C_\mu(y) = 1.0$. Linear dimensions are in meters.

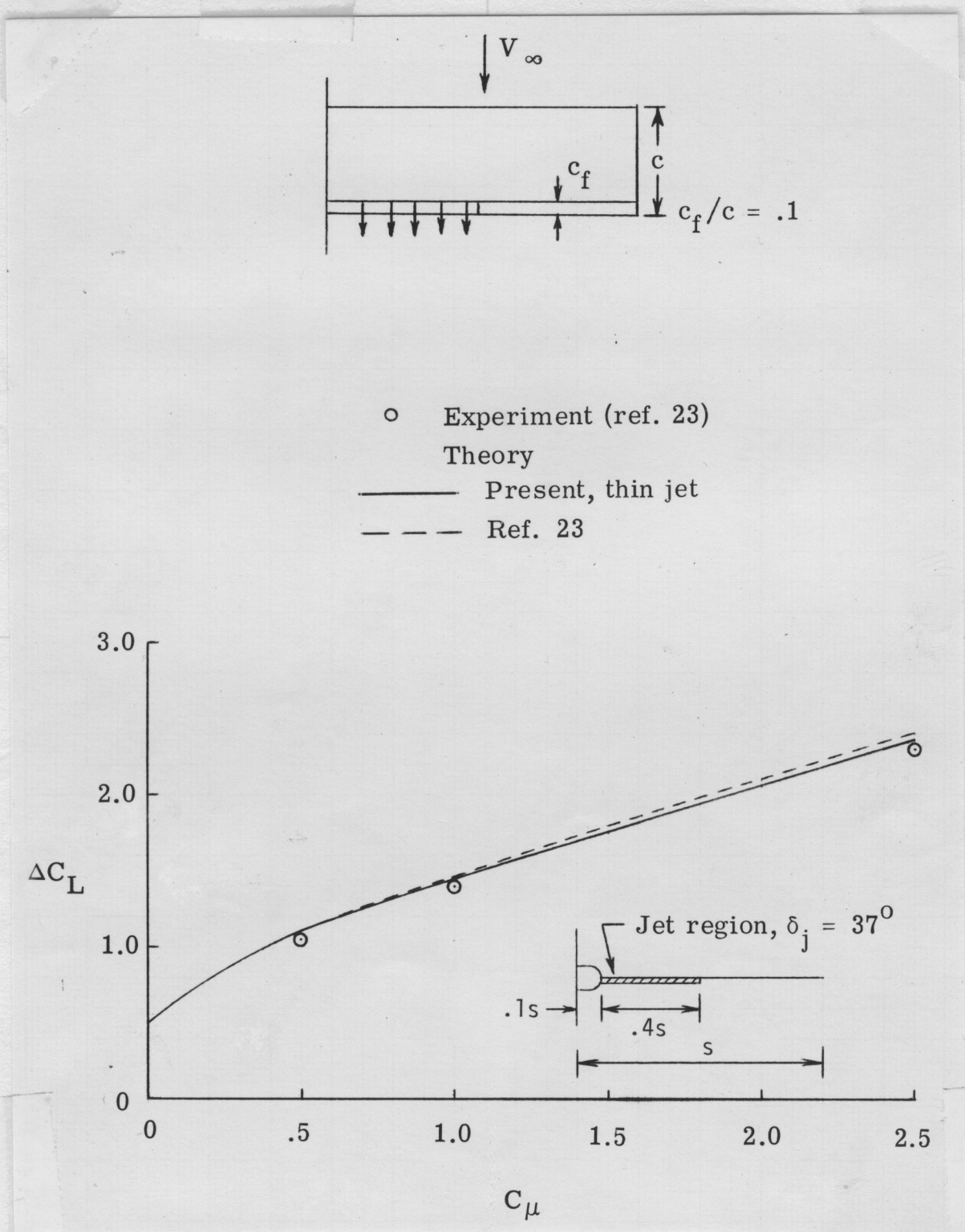

Figure 3.- Lift increment due to partial-span flap and blowing jet. $\alpha = 0^o$, AR = 6.

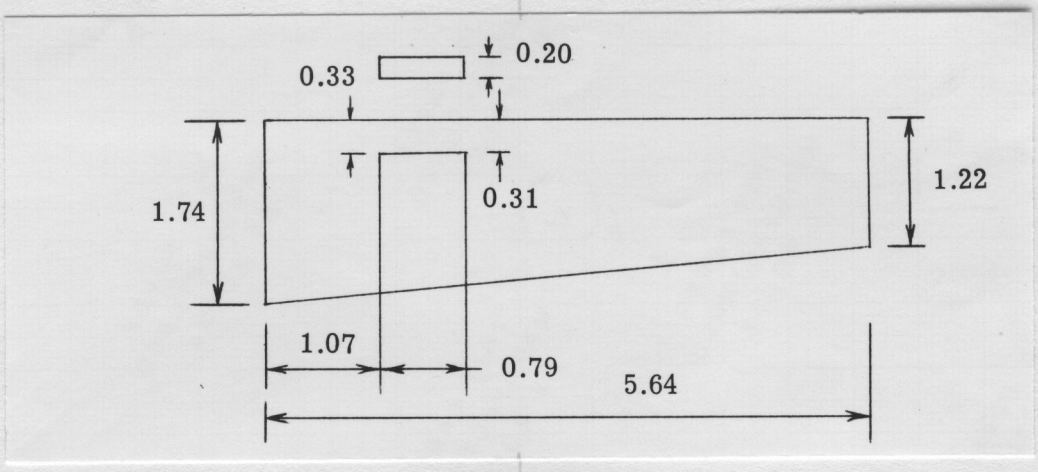

(a) Planform.

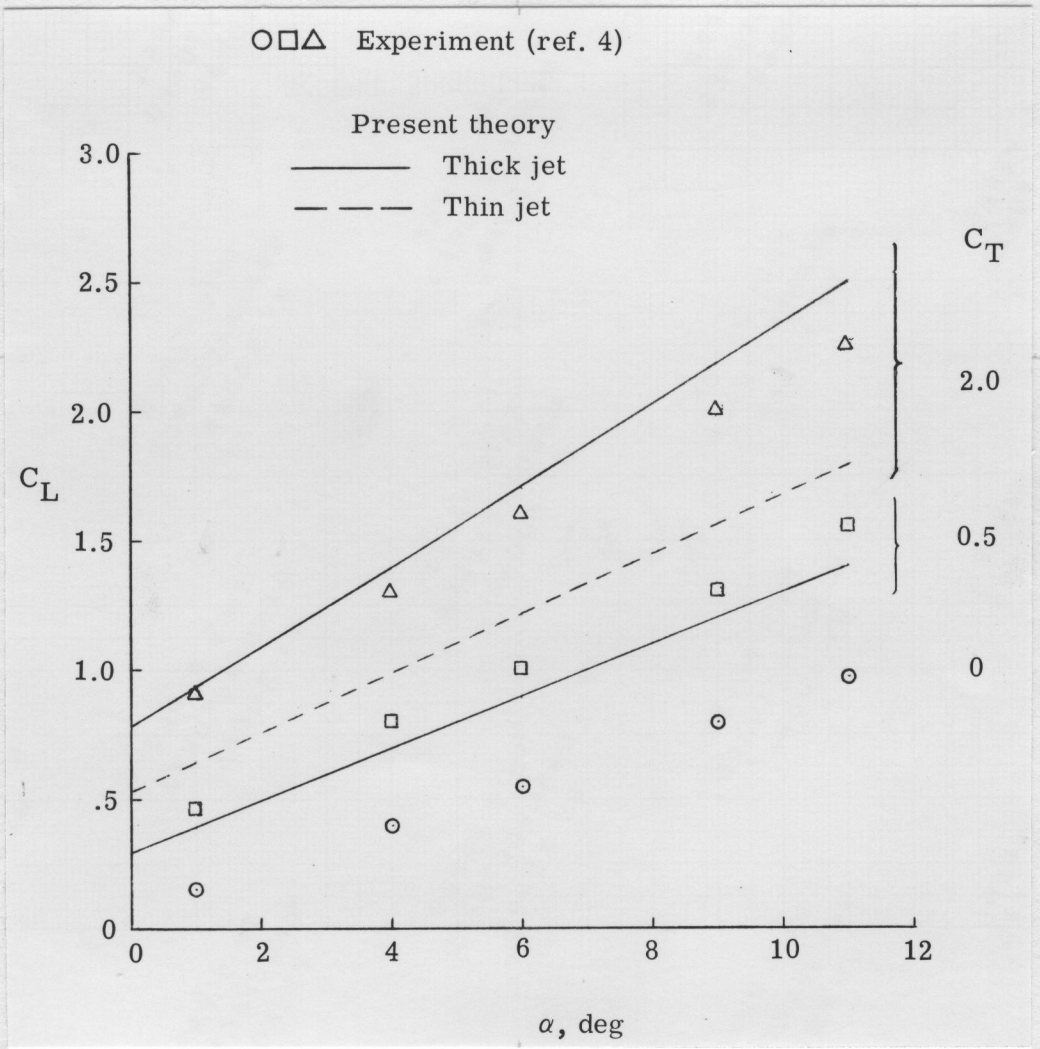

(b) Lift curves.

Figure 4.- Comparison of predicted lift curves with experiment for the USB configuration of reference 4. $\delta_f = 0^o$, $\delta_j = 12^o$, $M_o = M_j = 0$. Linear dimensions are in meters.

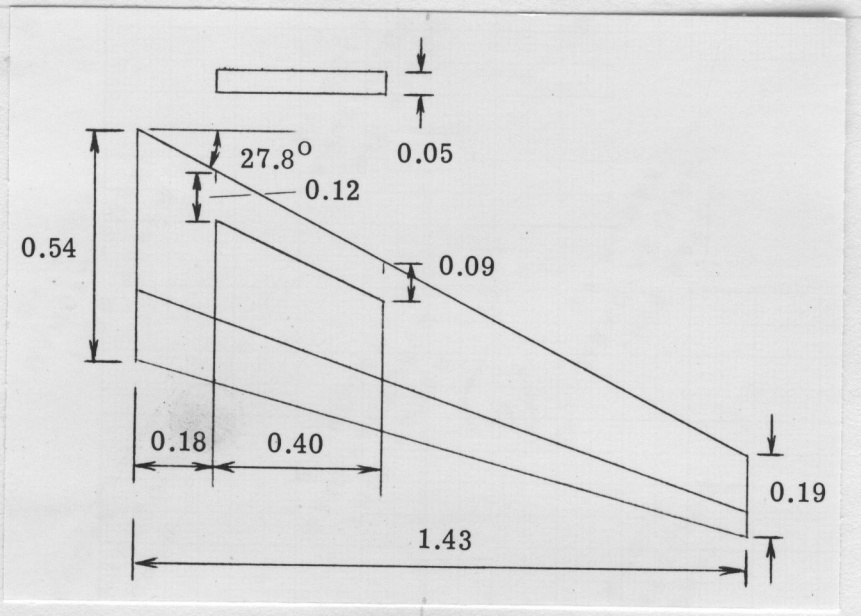

(a) Planform.

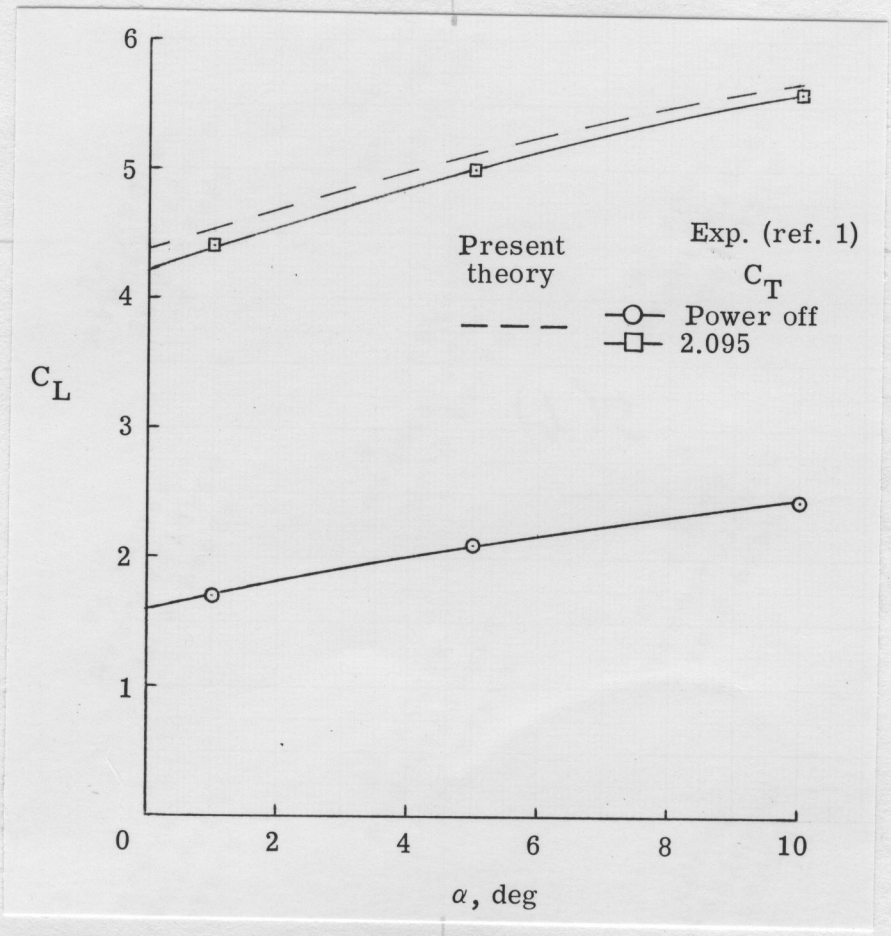

(b) Lift curves.

Figure 5.- Comparison of predicted lift curves with experiment for the USB configuration of reference 1. $M_o = M_j = 0$, $\delta_f = \delta_j = 30^o$, $AR = 7.79$, $\frac{c_f}{c} = 0.3$, NACA 65_1-412 airfoil. Linear dimensions are in meters.

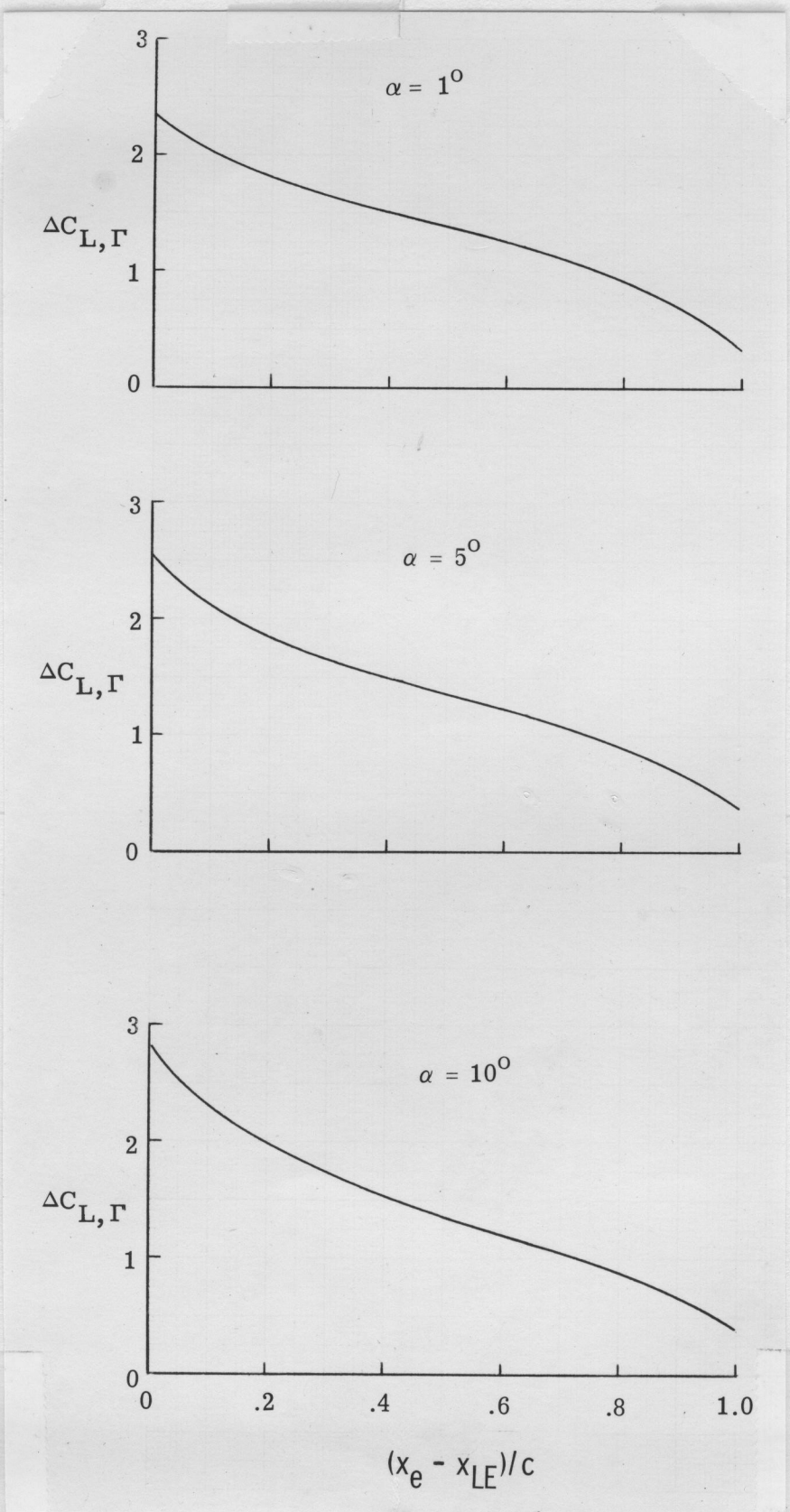

Figure 6.- Theoretical effects of chordwise location of jet exit on lift augmentation for configuration of figure 5(a). $\delta_f = 30^o$, $M_o = M_j = 0$, $C_T = 2.095$.

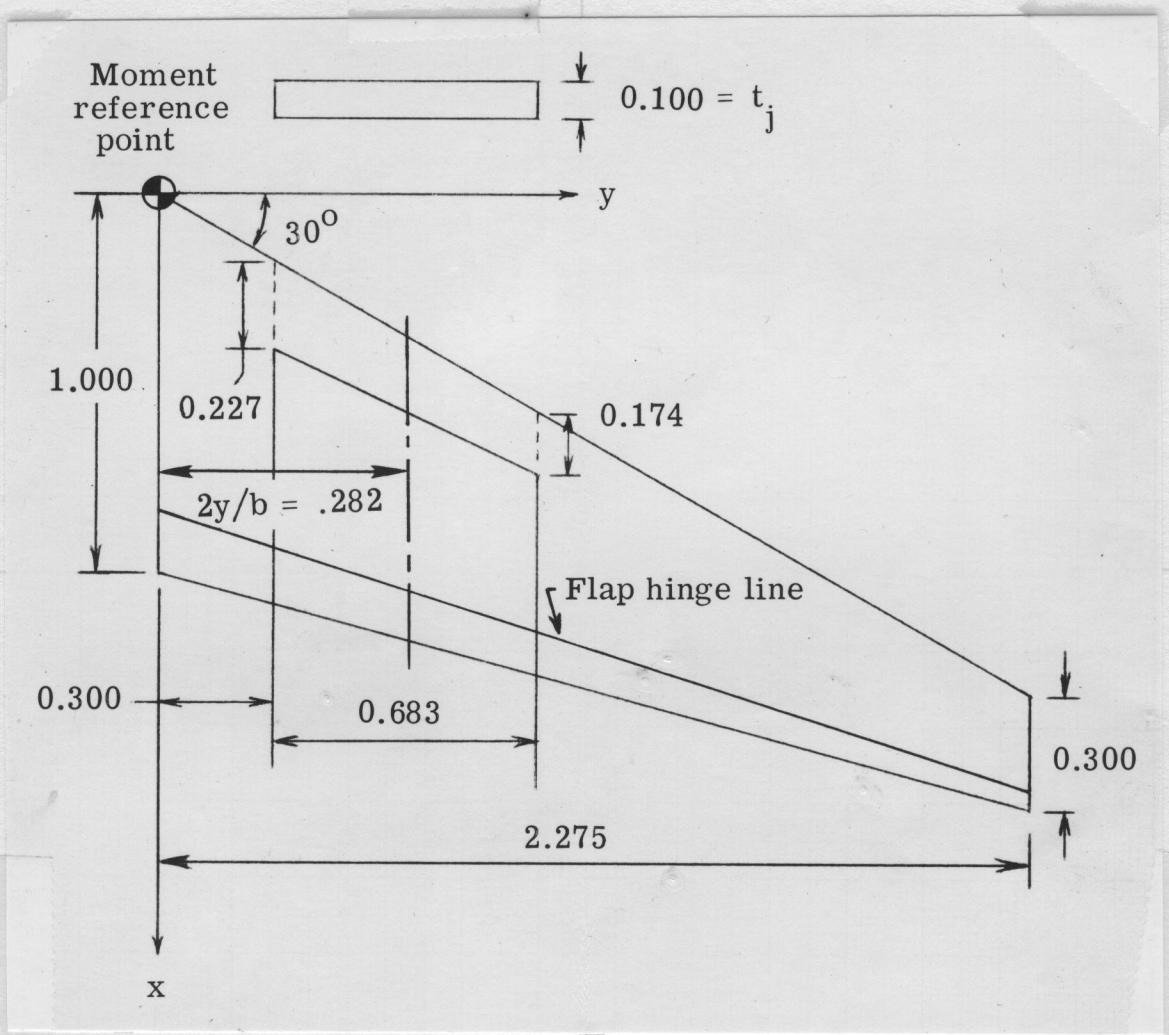

Figure 7.- Planform geometry for parametric investigation. AR = 7, NACA 65_1-412 airfoil. Linear dimensions are in meters.

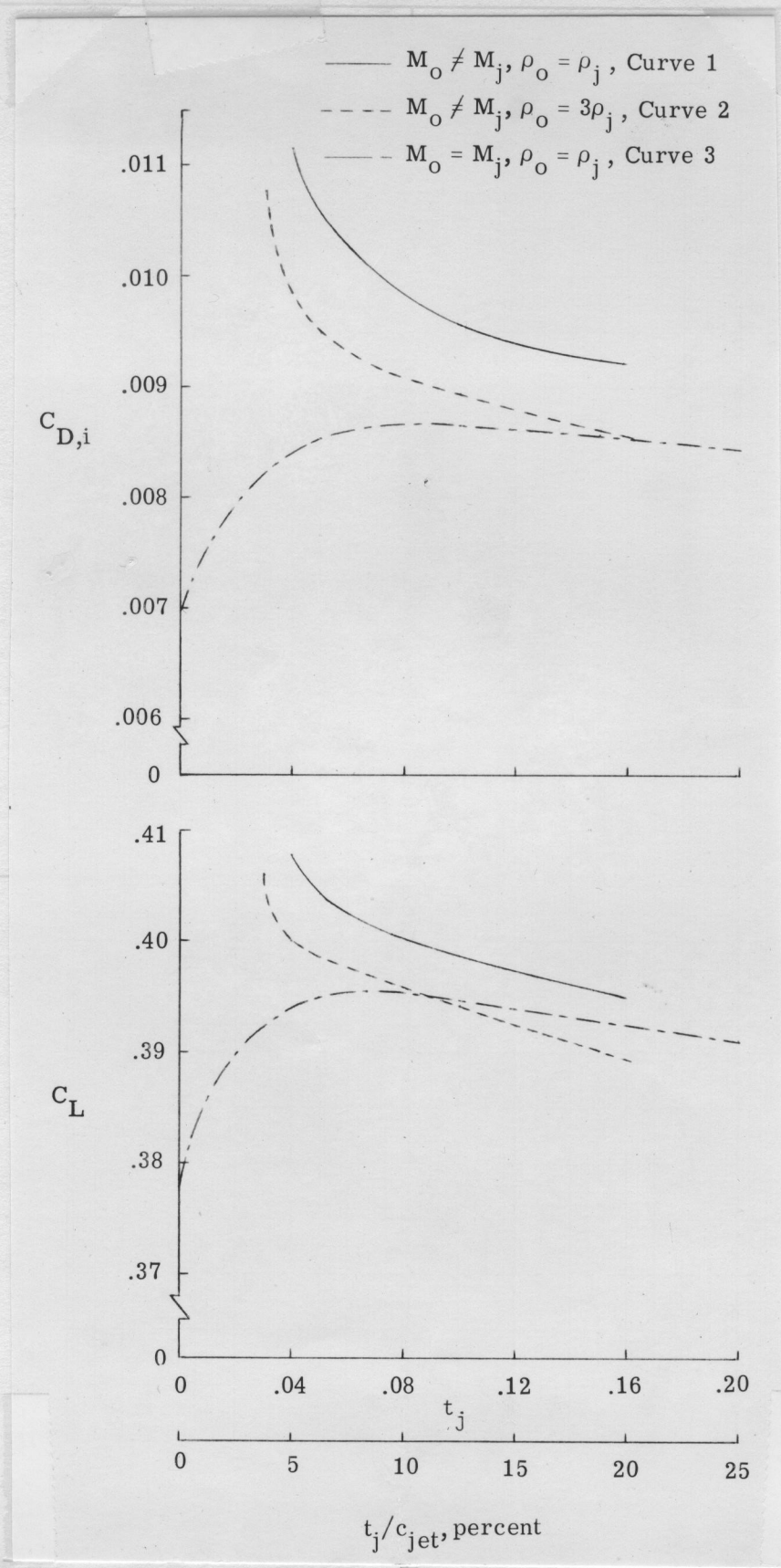

Figure 8.- Effects of jet thickness, temperature, and Mach number nonuniformity on C_L and $C_{D,i}$ for planform of figure 7 with flat airfoil. Jet exit at 0.25c, $M_o = 0.3$, $\alpha = 5^o$, and $C_T = 0.2$.

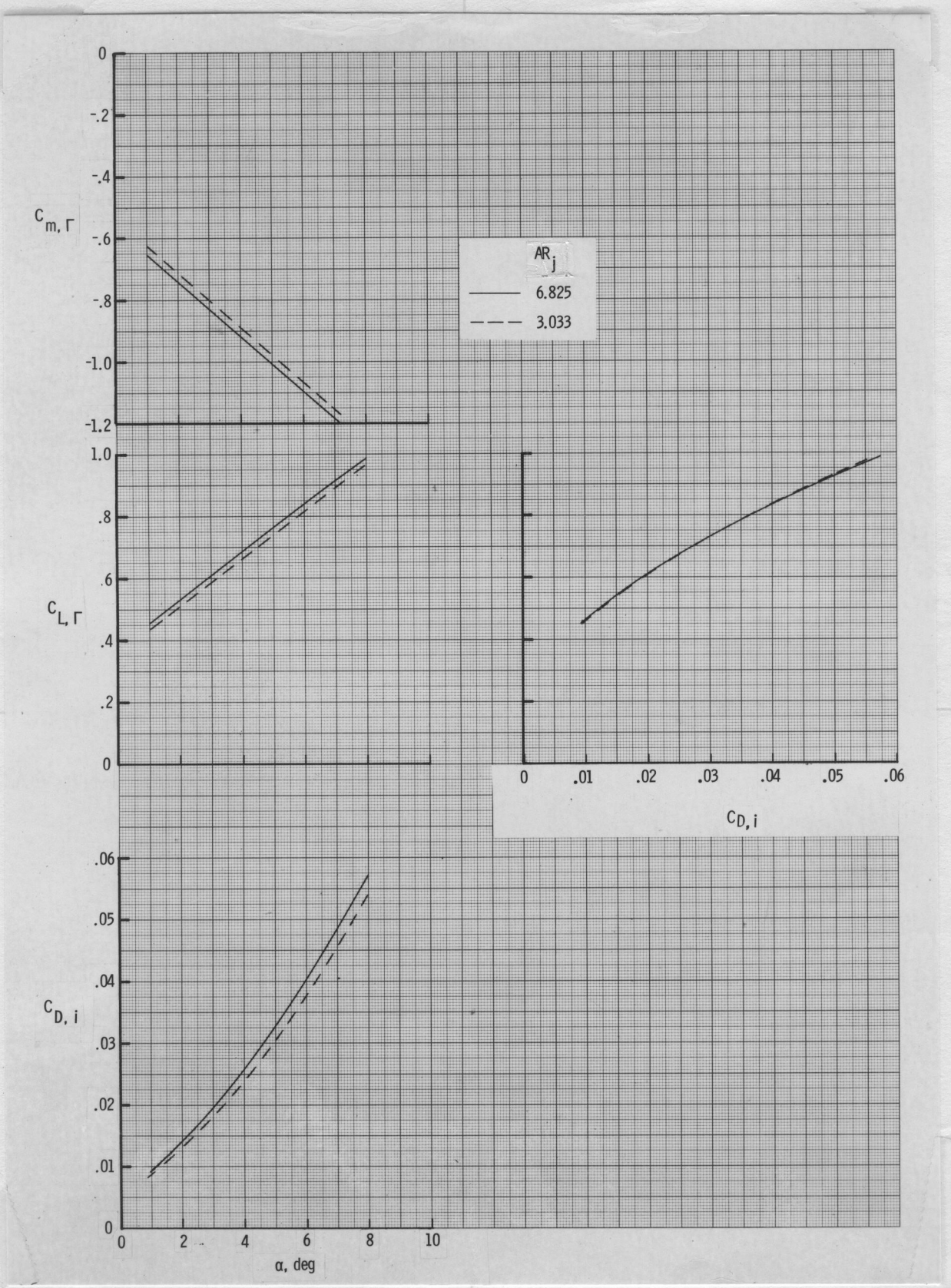

Figure 9.- Theoretical effects of jet aspect ratio on aerodynamic characteristics of configuration in figure 7. Jet exit at 0.25c, $C_T = 0.2$, $\delta_j = 10^o$, and $M_o = 0.3$.

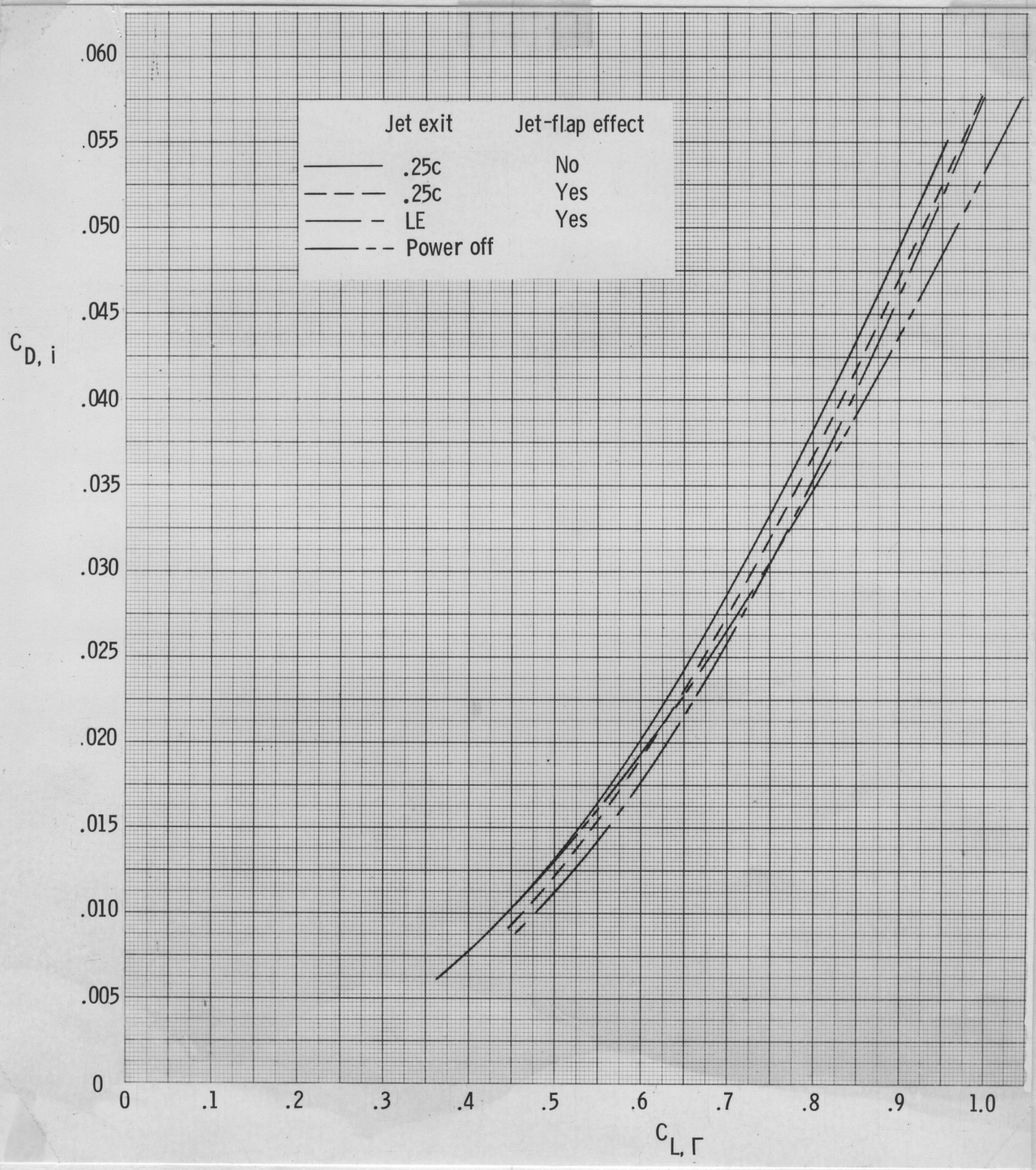

Figure 10.- Comparison of theoretical cruise performances for the cambered wing of figure 7 with and without jet-flap effect. $M_o = 0.3$, $M_j \neq M_o$, $\rho_o = 3\rho_j$, and $C_T = 0.2$.

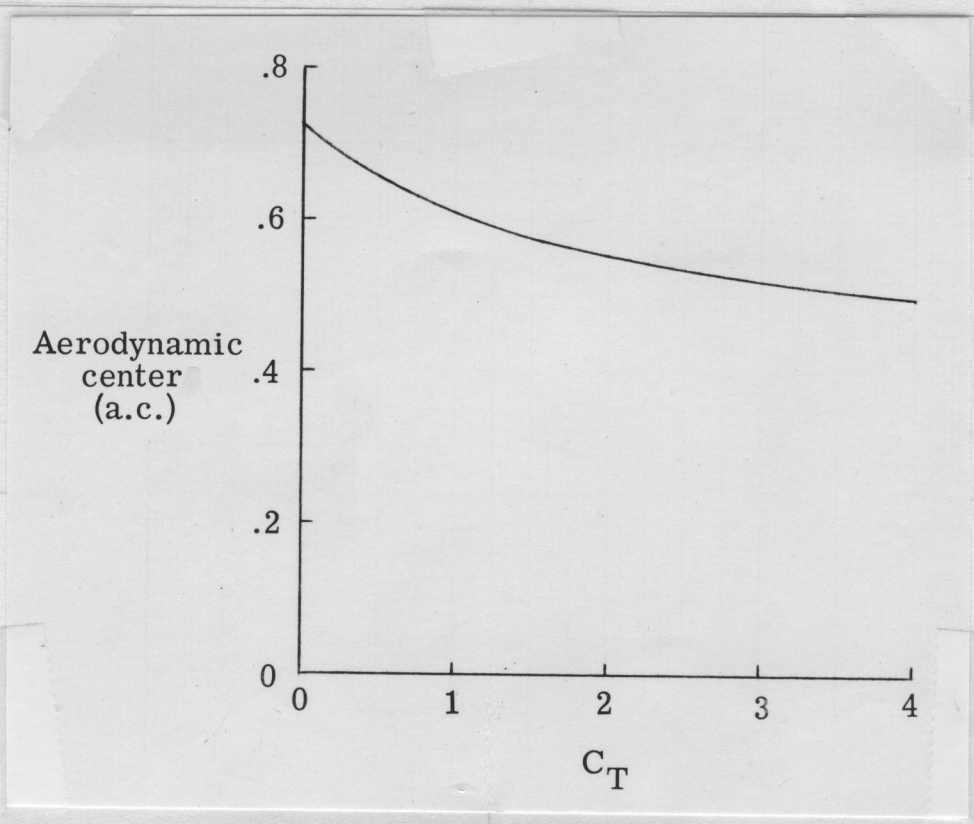

Figure 11.- Power effect on aerodynamic-center location for configuration of figure 7. $\frac{c_f}{c} = 0.3$, $\delta_f = 30^o$, and $M_o = M_j = 0$. (Jet-reaction effect not included.)

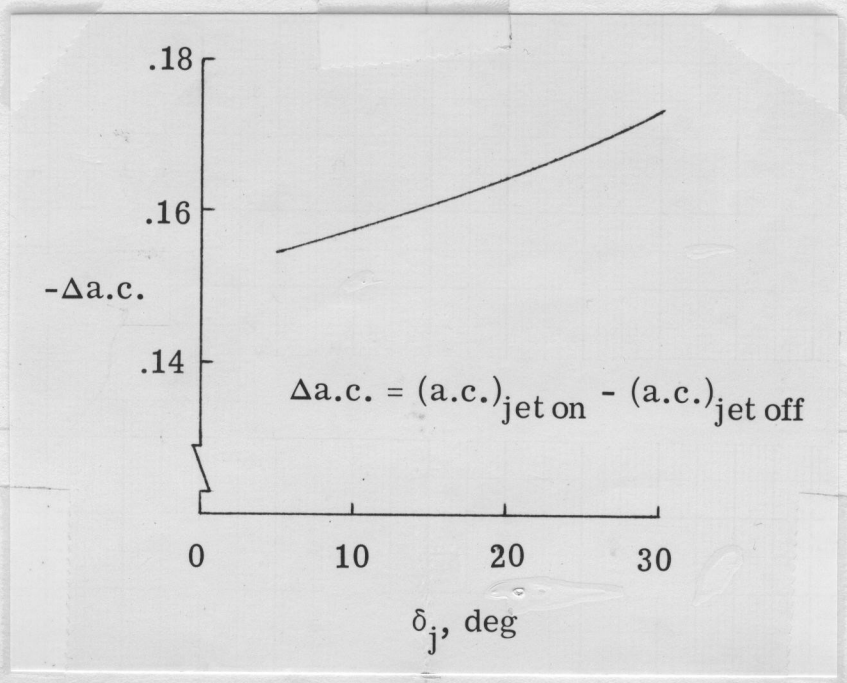

Figure 12.- Effect of jet deflection on aerodynamic-center location for configuration of figure 7. $\frac{c_f}{c} = 0.3$, $C_T = 2.0$, and $M_o = M_j = 0$. (Jet-reaction effect not included.)

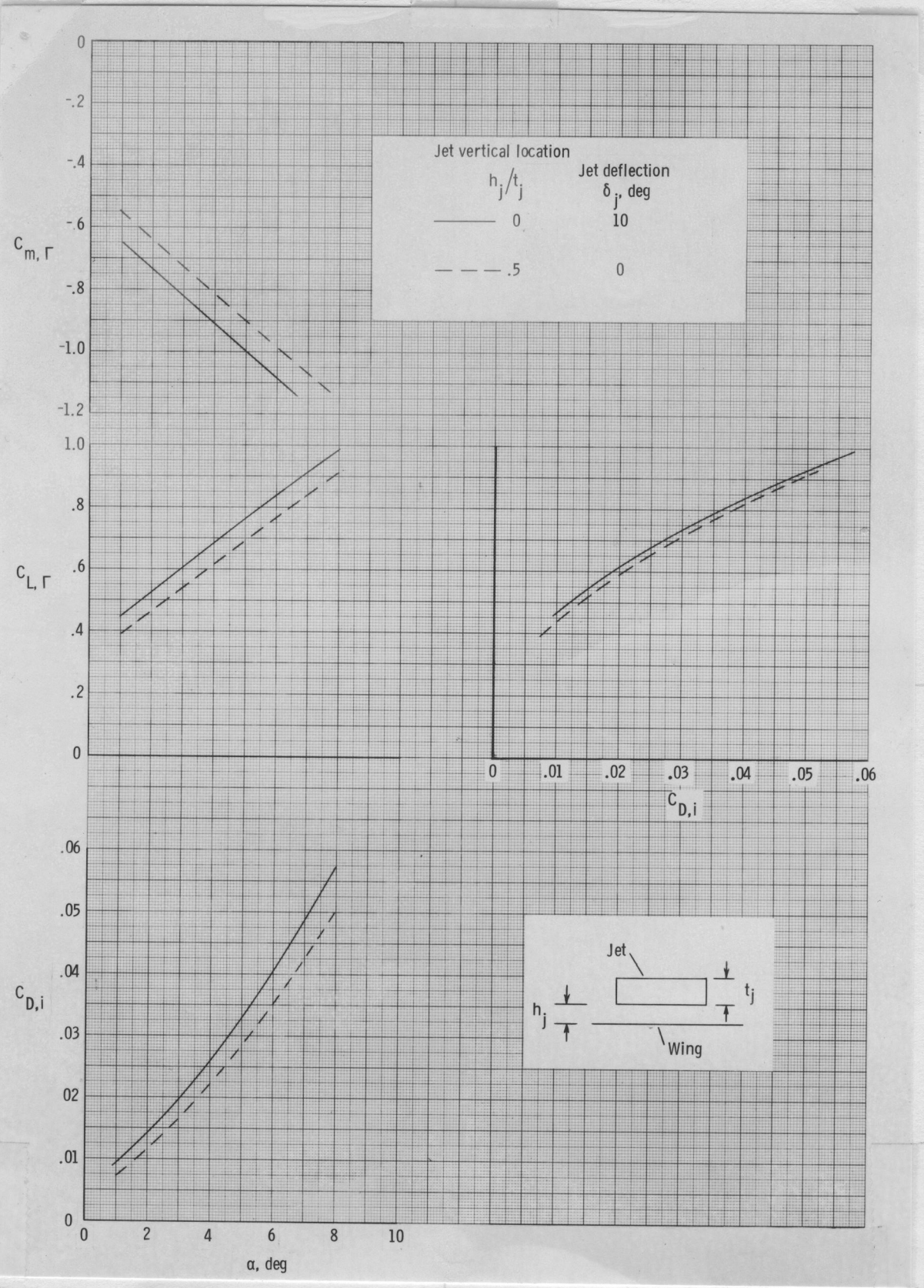

Figure 13.- Theoretical effects of jet vertical location on aerodynamic characteristics for the configuration of figure 7. Jet exit at 0.25c, $C_T = 0.2$, $M_o = M_j = 0.3$.

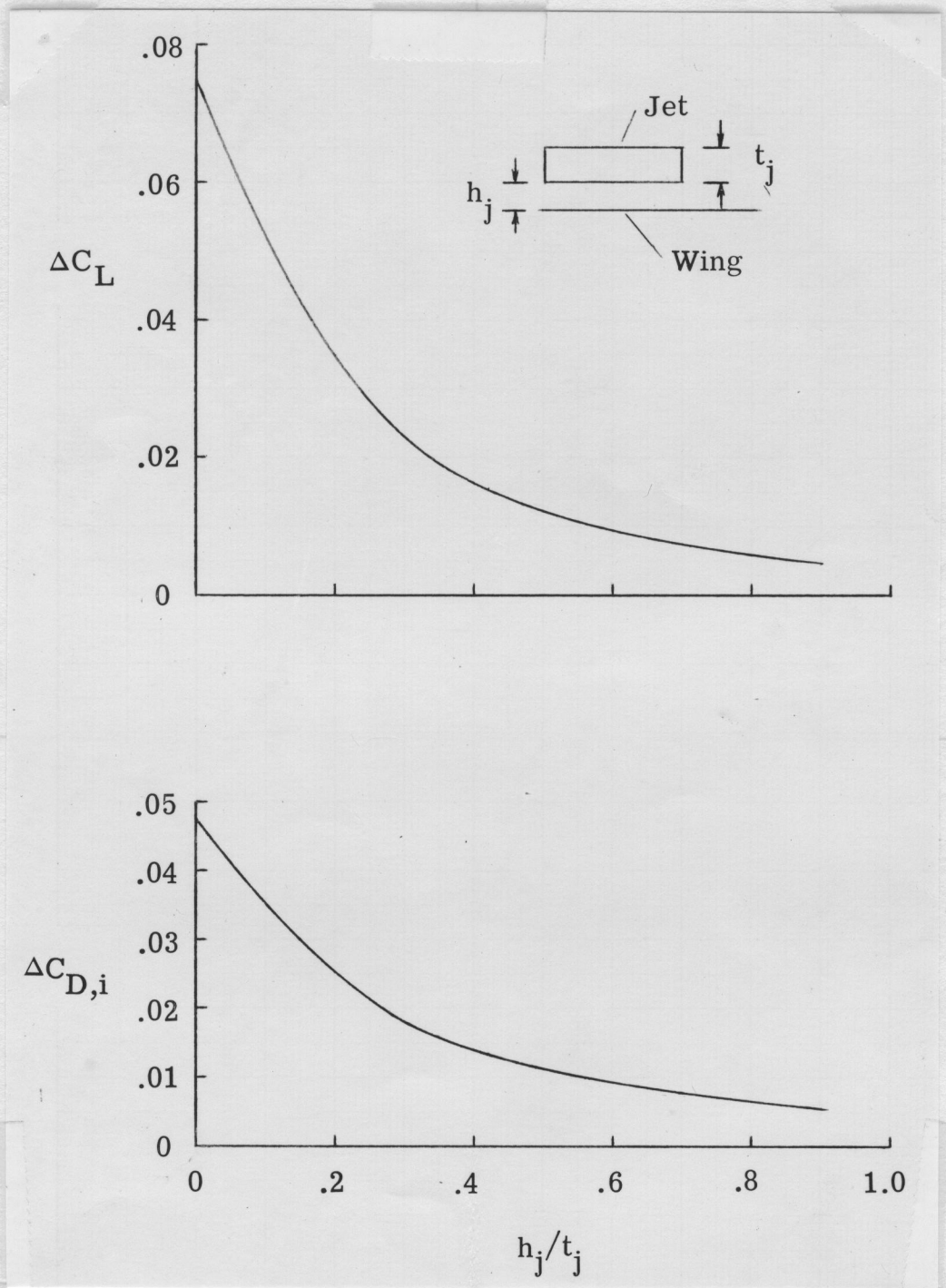

Figure 14.- Theoretical change in aerodynamic characteristics due to vertical shift of jet for configuration of figure 5(a). $\delta_j = \delta_f = 0^o$, $\alpha = 5^o$, $C_T = 2.095$, and $M_o = M_j = 0$. Jet exit at the leading edge.

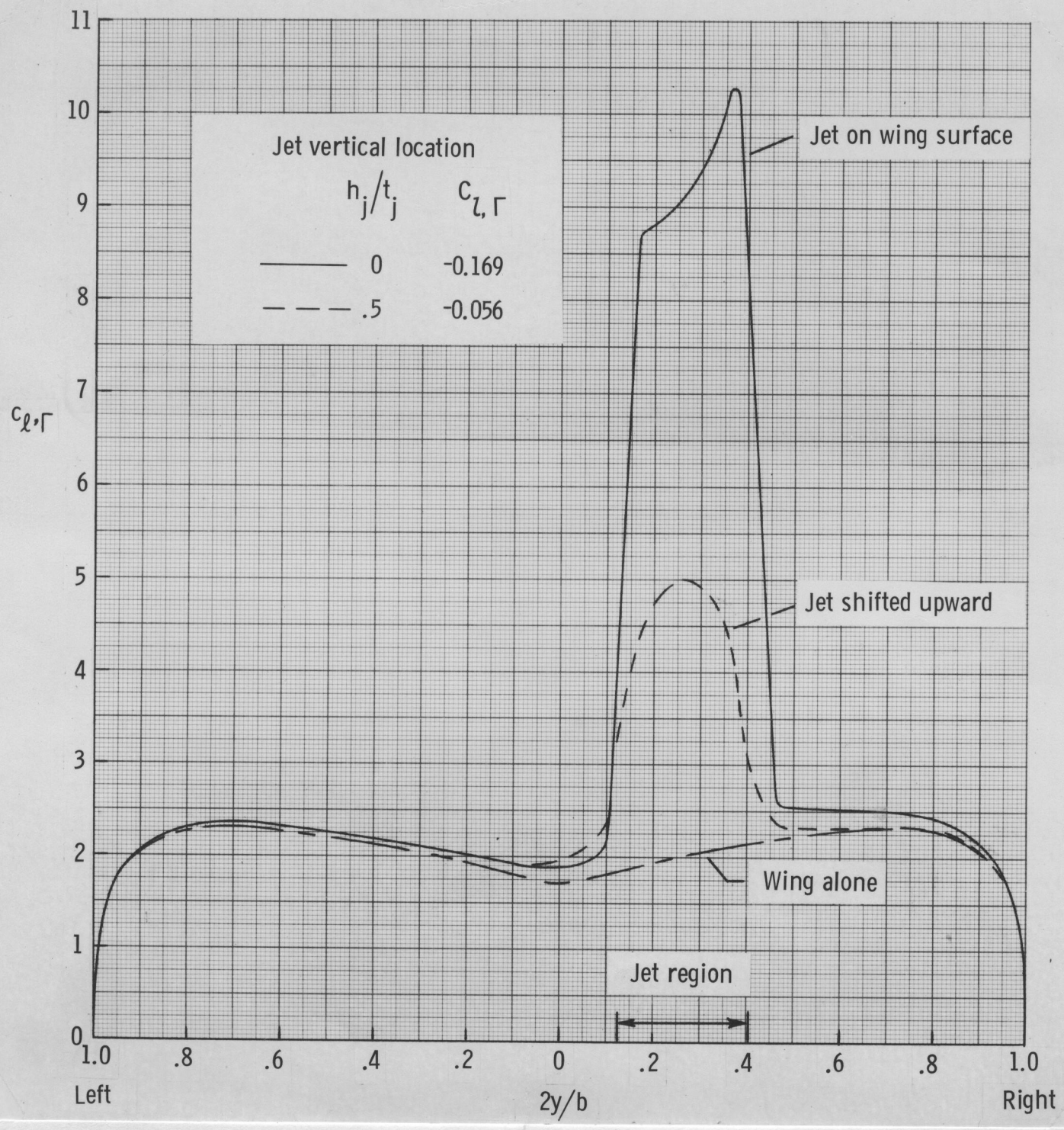

Figure 15.- Theoretical effects of jet vertical location on span loading and rolling moment for configuration of figure 5(a) with jet exit at leading edge and left engine inoperative. $\alpha = 5^{o}$, $\delta_j = \delta_f = 30^{o}$, and $C_T = 2.095$.

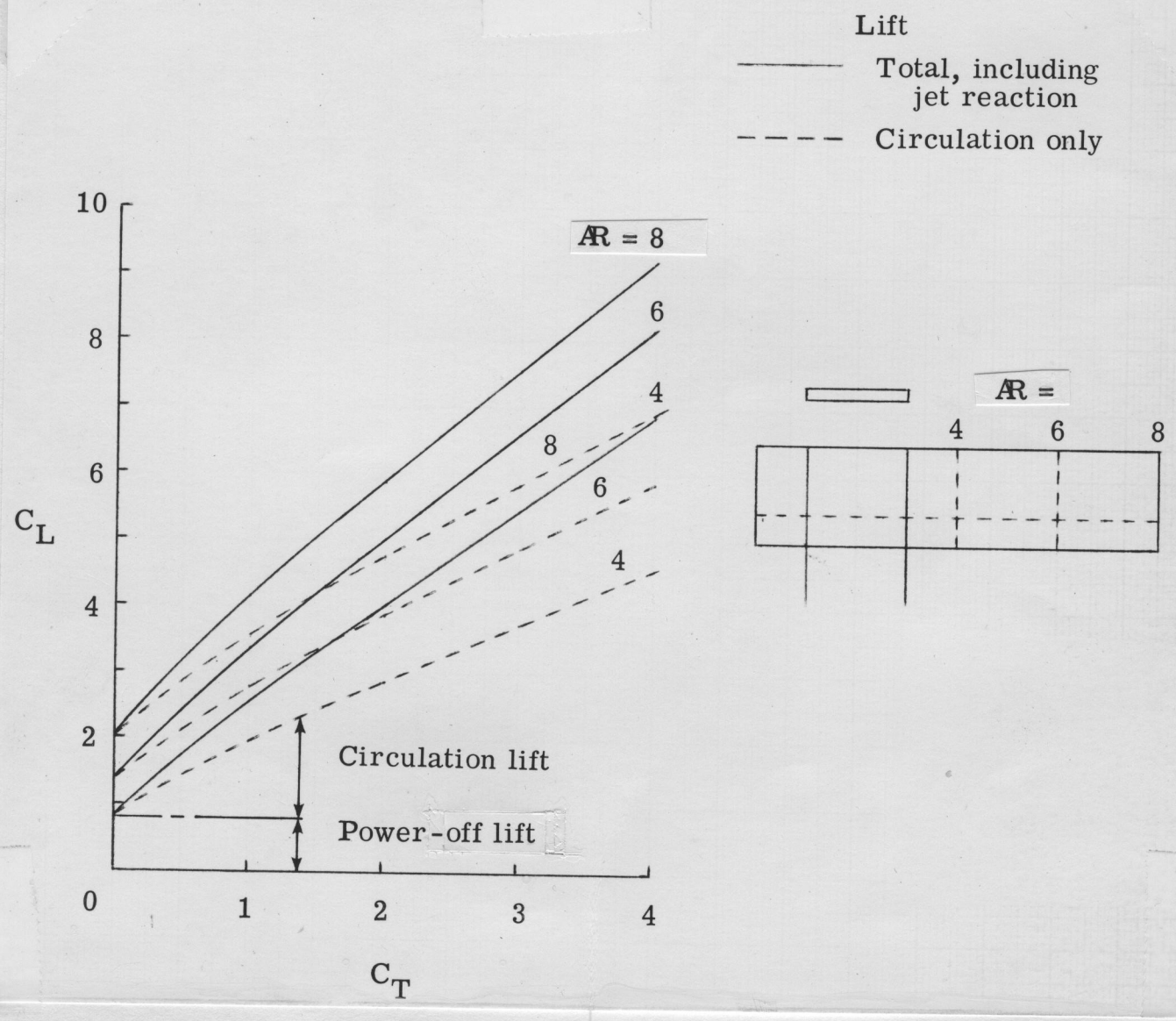

Figure 16.- Effects of wing aspect ratio on lift augmentation of rectangular planforms with USB jet. $\frac{c_f}{c} = 0.3$, $\delta_j = \delta_f = 30^o$, $\alpha = 5^o$, and $M_o = M_j = 0$. Jet exit at the leading edge, NACA 65_1-412 airfoil. (Results are based on wing area of AR = 8.)